The Astrophysical Journal, 976:231 (17pp), 2024 December 1 https://doi.org/10.3847/1538-4357/ad8915

A Photochemical Phosphorus-Hydrogen-Oxygen Network for Hydrogen-dominated Exoplanet Atmospheres

Elspeth K. H. Lee[1], Shang-Min Tsai[2], Julianne I. Moses[3], John M. C. Plane[4], Channon Visscher[3,5], and Stephen J. Klippenstein[6]
[1] Center for Space and Habitability, University of Bern, Gesellschaftsstrasse 6, CH-3012 Bern, Switzerland; elspeth.lee@unibe.ch
[2] Department of Earth Sciences, University of California, Riverside, CA 92521, USA
[3] Space Science Institute, Boulder, CO 80301, USA
[4] School of Chemistry, University of Leeds, Leeds LS2 9JT, UK
[5] Department of Chemistry, Dordt University, Sioux Center, IA 51250, USA
[6] Chemical Sciences and Engineering Division, Argonne National Laboratory, Lemont, IL 60439, USA
Received 2024 July 12; revised 2024 October 3; accepted 2024 October 19; published 2024 November 26

Abstract

Due to the detection of phosphine (PH_3) in the solar system gas giants Jupiter and Saturn, PH_3 has long been suggested to be detectable in exosolar substellar atmospheres too. However, to date, direct detection of phosphine has proven to be elusive in exoplanet atmosphere surveys. We construct an updated phosphorus-hydrogen-oxygen (PHO) photochemical network suitable for the simulation of gas giant hydrogen-dominated atmospheres. Using this network, we examine PHO photochemistry in hot Jupiter and warm Neptune exoplanet atmospheres at solar and enriched metallicities. Our results show for HD 189733b-like hot Jupiters that HOPO, PO, and P_2 are typically the dominant P carriers at pressures important for transit and emission spectra, rather than PH_3. For GJ1214b-like warm Neptune atmospheres our results suggest that at solar metallicity PH_3 is dominant in the absence of photochemistry, but is generally not in high abundance for all other chemical environments. At 10 and 100 times solar, small oxygenated phosphorus molecules such as HOPO and PO dominate for both thermochemical and photochemical simulations. The network is able to reproduce well the observed PH_3 abundances on Jupiter and Saturn. Despite progress in improving the accuracy of the PHO network, large portions of the reaction rate data remain with approximate, uncertain, or missing values, which could change the conclusions of the current study significantly. Improving understanding of the kinetics of phosphorus-bearing chemical reactions will be a key undertaking for astronomers aiming to detect phosphine and other phosphorus species in both rocky and gaseous exoplanetary atmospheres in the near future.

Unified Astronomy Thesaurus concepts: Exoplanet atmospheric composition (2021); Atmospheric composition (2120); Chemical kinetics (2233)

1. Introduction

Phosphine (PH3) has been detected in the gas giants of the solar system since the 1970s, in Jupiter (S. Ridgway et al. 1976; S. T. Ridgway et al. 1976) and Saturn (J. D. Bregman et al. 1975), providing strong evidence of nonequilibrium chemistry and vertical mixing occurring in their atmospheres, as P_4O_6 was the expected dominant P carrier at Jupiter/Saturn's photospheric temperatures at chemical equilibrium (e.g., B. J. Fegley & R. G. Prinn 1985; B. J. Fegley & K. Lodders 1994; C. Visscher & B. J. Fegley 2005).

Initial chemical kinetic modeling of phosphorous species in the atmospheres of Jupiter and Saturn began with R. G. Prinn & J. S. Lewis (1975), using available experimental data at the time and investigated the formation pathways of P_4 and solid P_4(s) from the initial photodissociation of PH_3. Later models focused on the coupled photochemistry of PH_3 and NH_3 and the likelihood of diphosphine (P_2H_4) as the primary phosphorus-containing tropospheric aerosol on the Jovian planets (D. F. Strobel 1977; J. A. Kaye & D. F. Strobel 1983, 1984; S. G. Edgington et al. 1998). More recent studies of the nonequilibrium abundance of PH_3 on Jupiter and Saturn emphasize different quench pathways, rate-limiting reactions, and important P-bearing species (D. Wang et al. 2016).

Outward from the context of solar system gas giants, phosphine was also expected to be present and detectable in brown dwarf and hydrogen-dominated exoplanet atmospheres (B. J. Fegley & K. Lodders 1996; C. Visscher et al. 2006). However, to date, direct detection of PH_3 in brown dwarf atmospheres has proven elusive. Several studies where PH_3 was expected to be detected in the brown dwarf regime failed to detect signatures of PH_3 absorption (e.g., C. V. Morley et al. 2018; B. E. Miles et al. 2020; S. A. Beiler et al. 2023). With the advent of the JWST telescope, which can now distinguish signatures of trace gas phase species such as SO_2 in warm Saturn atmospheres (L. Alderson et al. 2023; Z. Rustamkulov et al. 2023; D. Powell et al. 2024), there is an opportunity to detect PH_3 signatures and other trace phosphorus-bearing species in exoplanet atmospheres with more clarity.

Phosphine has long been suggested to be a biomarker indicator due to the importance of phosphorus to the functioning and development of Earth-based biological organisms (e.g., C. Sousa-Silva et al. 2020). Phosphorus has a wide range of redox states (M. A. Pasek et al. 2017) and the accumulation of phosphate seems to be key to the origin of life (J. D. Toner & D. C. Catling 2019). Simulations performed by D. Angerhausen et al. (2023) suggest that the proposed ESA LIFE mission (S. P. Quanz et al. 2022) will be able to detect

PH_3 in cold super-Earth and Jupiter-like exoplanets in under one hour of observing time. For smaller planets, their simulations suggest ten hours of observing time to detect PH_3.

Recently, hints for PH_3 production in Venus's atmosphere were seen in microwave measurements (J. S. Greaves et al. 2021),[7] which could not be explained by nonbiological kinetic modeling alone (W. Bains et al. 2021). If PH_3 production occurs, it suggests that active biology or unknown abiotic chemistry may be occurring in the upper atmosphere of Venus. However, full confirmation and an accurate determination of PH_3 abundance and vertical profile (A. P. Lincowski et al. 2021) on Venus may need to wait for proposed Venus orbiter and probe missions (e.g., R. Ghail et al. 2017; J. B. Garvin et al. 2022) and other dedicated search efforts.

In summary, from the above studies, PH_3 is a key molecule to explore and search for across the planetary parameter regime. From large gas giants to small rocky planets, understanding the formation chemistry of PH_3 and other P-bearing molecules will be a significant goal for astronomers in the near and long term.

To start to meet this challenge, in this study, we develop and investigate the properties of a phosphorus-hydrogen-oxygen (PHO) photochemical network suitable for hydrogen-dominated atmospheres. We aim to elucidate the mechanisms at play that give rise to PH_3 and other phosphorus species in exoplanet atmospheres and study the role of photochemistry in the PHO system. In Section 2, we provide details on the thermochemical, kinetic, and photochemical aspects of the proposed network. In Section 3, we compare the results of our thermochemical scheme to those presented in D. Wang et al. (2017). In Section 4, we apply our scheme to a canonical hot Jupiter atmosphere, examining the effects of photochemical processes on the P species in these atmospheres. In Section 5, we move to colder and small warm Neptune planets, examining the phosphorus content of their atmospheres, in particular the effects of metallicity on the dominant P species carriers. Section 6 applies the network to the deep atmospheres of Jupiter and Saturn. Section 7 contains a discussion of the results and the mechanisms, and Section 8 examines the potential observational impacts. Section 9 summarizes the conclusions of the study.

2. Development of an Exoplanet PHO Photochemical Network

To perform the kinetic modeling of the PHO network, we use the 1D photochemical model VULCAN (S.-M. Tsai et al. 2017, 2021) to integrate the network to a steady state. Throughout, we assume the solar elemental ratios (or some multiple factors thereof) from M. Asplund et al. (2021) for each element. Chemical equilibrium is assumed for each species as their initial conditions, which is performed using the FastChem (J. W. Stock et al. 2018) module of VULCAN. The PHO photochemical scheme and related data can be found as part of the publicly available VULCAN[8] code.

2.1. PHO Thermochemical Kinetics

The basis for the thermochemistry scheme comes from the network of D. Wang et al. (2016), originally designed to investigate PH_3 in the deep Jupiter and Saturn atmospheres and subsequently applied to hot Jupiter atmospheres in D. Wang et al. (2017). This primarily pulled data from the network of A. Twarowski (1995), developed for flame and ignition applications. However, A. Twarowski (1995) used Benson group-additivity rules (S. W. Benson & J. H. Buss 1958) to estimate the activation energies and also estimated the rate constants of the majority of their reaction list, therefore making the network highly approximate overall. Despite its approximate nature, the A. Twarowski (1995) network provides a useful basis for the construction of a phosphorus photochemical network suitable for exoplanet atmospheres and gives indications of the important chemical pathways that are required to be studied in more detail. For the phosphorous reactions, we take the reaction list used in D. Wang et al. (2016)[9] as an initial starting point for the PHO thermochemical network.

For the HO chemistry, we use the species and reactions from S.-M. Tsai et al. (2017, 2021; Appendix B). In addition, we include photolysis reactions for H_2O, H_2, OH, HO_2, and O_2 (Table 1).

Since A. Twarowski (1995), several studies have attempted to improve the accuracy of key reaction rates through various experimental and theoretical efforts. N. L. Haworth et al. (2002) and J. C. Mackie et al. (2002) investigated several uncertain phosphorus oxidation reactions using computational chemistry techniques and updated their rates. T. M. Jayaweera et al. (2005) updated several reactions from A. Twarowski (1995) with theoretically derived rates and estimations, mostly stemming from the results presented in P. Glaude et al. (2000). Several phosphorus oxidation reactions were also investigated experimentally by K. M. Douglas et al. (2019) and K. M. Douglas et al. (2020). These new rates were subsequently applied in stellar wind modeling (K. M. Douglas et al. 2022) and the modeling of P chemistry in the Earth's upper atmosphere, where P is produced by the ablation of

Table 1
List of Photolysis Reactions Used for the PHO Photochemical Network

Species	Reaction	Threshold (nm)	Cross Section/Branching Ratio References
H_2O	$\rightarrow H + OH$	207	A. N. Heays et al. (2017)
	$\rightarrow H_2 + O(^1D)$	...	W. F. Huebner & J. Mukherjee (2015)
	$\rightarrow O + H + H$	145	...
H_2	$\rightarrow H + H$	120	A. N. Heays et al. (2017)
OH	$\rightarrow H + O$	265	A. N. Heays et al. (2017)
HO_2	$\rightarrow O + OH$	275	A. N. Heays et al. (2017)
O_2	$\rightarrow O+O$	240	W. F. Huebner & J. Mukherjee (2015)
	$\rightarrow O + O(^1D)$	175.6	S. Sander et al. (2006)
PH	$\rightarrow P + H$	190	A. N. Heays et al. (2017)
PH_2	$\rightarrow PH + H$	299	This study
PH_3	$\rightarrow PH_2 + H$	230	F. Chen et al. (1991)
PO	$\rightarrow P + O$	184	This study
PO_2	$\rightarrow PO + O$	235	This study
HOPO	$\rightarrow PO_2 + H$	325.4	J. M. C. Plane et al. (2021)
$HOPO_2$	$\rightarrow PO_2 + OH$	271.2	J. M. C. Plane et al. (2021)
P_2	$\rightarrow P + P$	247	This study
P_2H_2	$\rightarrow PH + PH$	338	This study
P_2H_4	$\rightarrow PH_2 + PH_2$	508	This study

[7] Though not without controversy (e.g., T. Encrenaz et al. 2020; G. L. Villanueva et al. 2021).
[8] https://github.com/exoclime/VULCAN
[9] Which can be found on KIDA: https://kida.astrochem-tools.org/.

cosmic dust particles during atmospheric entry (J. M. C. Plane et al. 2021). L. Baptista & A. A. de Almeida (2023) calculated several high-pressure rates for PH_x decomposition reactions.

In addition to incorporating updated rates from the above studies, we have also produced new theoretical rate coefficients for some key reactions:

$$H + PH_3 \rightarrow H_2 + PH_2, \quad \text{(R55)}$$
$$H + PH_2 \rightarrow H_2 + PH, \quad \text{(R57)}$$
$$H + PH \rightarrow P + H_2, \quad \text{(R59)}$$
$$P + PH \rightarrow H + P_2, \quad \text{(R281)}$$
$$PH_2 + PH \rightarrow P + PH_3, \quad \text{(R293)}$$
$$H + PH_2 + M \rightarrow PH_3 + M, \quad \text{(R329)}$$
$$H + P_2 + M \rightarrow P_2H + M, \quad \text{(R335)}$$
$$PO + PO_2 + M \rightarrow P_2O_3 + M, \quad \text{(R337)}$$
$$H + PH + M \rightarrow PH_2 + M, \quad \text{(R341)}$$
$$P_2O_3 + P_2O_3 + M \rightarrow P_4O_6 + M. \quad \text{(R349)}$$

Notably, we have included a theoretical reaction rate to form P_4O_6 from the recombination reaction R349, which is detailed in Appendix A. Furthermore, we have also included estimates for the reaction rates involving the formation of P_2H_2 and P_2H_4 based on their nitrogen counterparts (Appendix B). Overall, we have devised a PHO network that replaces around 25% of the original A. Twarowski (1995)/D. Wang et al. (2016) network, amounting to a total of 32 species with 195 forward reactions (390 total including reverse reactions) plus 18 irreversible photochemical reactions. Appendix B (Tables 3 and 4) presents the list of reactions in the PHO network and their rate coefficients.

2.1.1. Phosphorus Thermochemical Data

A large area of uncertainty in the chemical modeling of phosphorus species is the accuracy of available thermochemical data and the choice of database. Of note are the different values adopted for the P_4O_6 enthalpy of formation, as using different sources changes the expected equilibrium distribution of P-bearing species at cooler temperatures (see discussion in B. J. Fegley & K. Lodders 1994; S. Borunov et al. 1995; D. Wang et al. 2016; C. Visscher 2020). For example, at temperatures relevant to Jupiter's and Saturn's deep atmosphere, the expected dominant P-bearing gas at equilibrium can be P_4O_6 (using P_4O_6 enthalpy values from NIST-JANAF; M. Chase 1998) or H_3PO_4 (using P_4O_6 enthalpy values from L. V. Gurvich et al. 1989).

D. Wang et al. (2016) also discuss this discrepancy, opting for the thermodynamic data from L. V. Gurvich et al. (1989) as incorporated into the NASA thermodynamic polynomials (e.g., B. J. McBride & S. Gordon 1992; M. J. Zehe et al. 2002), which favors the formation of H_3PO_4 at low temperatures. Recently, the W. Bains et al. (2023) review of P_4O_6 thermochemistry suggests that the commonly used NIST-JANAF database (M. Chase 1998) values for the free energy of formation of P_4O_6 are likely too low and the molecule is less stable than the NIST-JANAF values suggest. In addition, K. Lodders (1999) updated the thermochemical properties of PH, PH_3, and PN with the white phosphorus reference state, which were not corrected in the NIST-JANAF database (M. Chase 1998).

In the present work, we likewise adopt thermodynamic values from the NASA database (including P_4O_6 enthalpy data from the Gurvich database; B. J. McBride & S. Gordon 1992; M. J. Zehe et al. 2002) and A. Burcat & B. Ruscic (2005) for simplicity and consistency between D. Wang et al. (2017) and our study. These values are also used in the FastChem (J. W. Stock et al. 2018) module to VULCAN, which calculates the initial conditions of each species in chemical equilibrium.

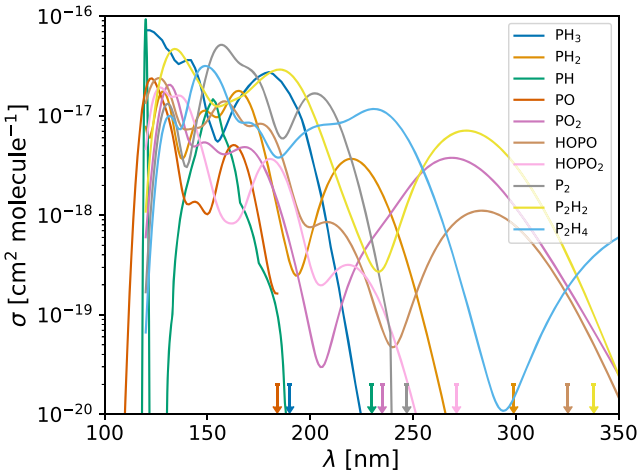

Figure 1. UV absorption cross sections for the phosphorus species in the network that undergo photolysis reactions. The photolysis threshold wavelength for each species is indicated by the colored arrows.

2.2. PHO Photochemistry

For the PHO photochemical network, we include several photolysis reactions listed in Table 1. We take UV cross sections from the PhiDrates (W. F. Huebner & J. Mukherjee 2015) and Leiden Observatory (A. N. Heays et al. 2017) databases, with the PH_3 UV cross sections taken from F. Chen et al. (1991). HOPO and $HOPO_2$ cross sections are taken from the theoretical calculations of J. M. C. Plane et al. (2021). We also calculate new theoretical UV cross sections and threshold wavelengths for PH_2, PO, PO_2, P_2, P_2H_2, and P_2H_4 (Appendix A). In Figure 1, we show the UV photoabsorption cross sections and threshold wavelengths of each of the phosphorus species that undergo photolysis. This expands the total number of photolysis reactions involving P to 10.

3. Comparison to D. Wang et al. (2017)

In this section, we compare our thermochemical kinetics and transport scheme to that of D. Wang et al. (2017), who applied the network of D. Wang et al. (2016) to various exoplanet temperature–pressure (T–p) profiles and vertical mixing rate scenarios. In Figure 2, we show the results of the $T_{eq} = 500$, 1000, 1500, and 2000 K hot Jupiter models that use the same T–p profiles as in D. Wang et al. (2017) and $K_{zz} = 10^9$ cm^2 s^{-1} at solar metallicity. Our results agree well across all equilibrium temperatures, with the major difference being the abundance of H_3PO_4 in the 1500 and 2000 K profiles. However, the volume mixing ratio (VMR) of H_3PO_4 is extremely small here and in D. Wang et al. (2017), making it a very minor species at these higher temperatures. Other minor differences are in the oxygenated phosphorus species such as HOPO, which we produce slightly less of. We attribute this difference to the updated reaction rates used here, which results in a reduction in the number of oxygen radicals able to oxidize P, as well as the specific updated rates for the formation of HOPO and other oxygenated P molecules.

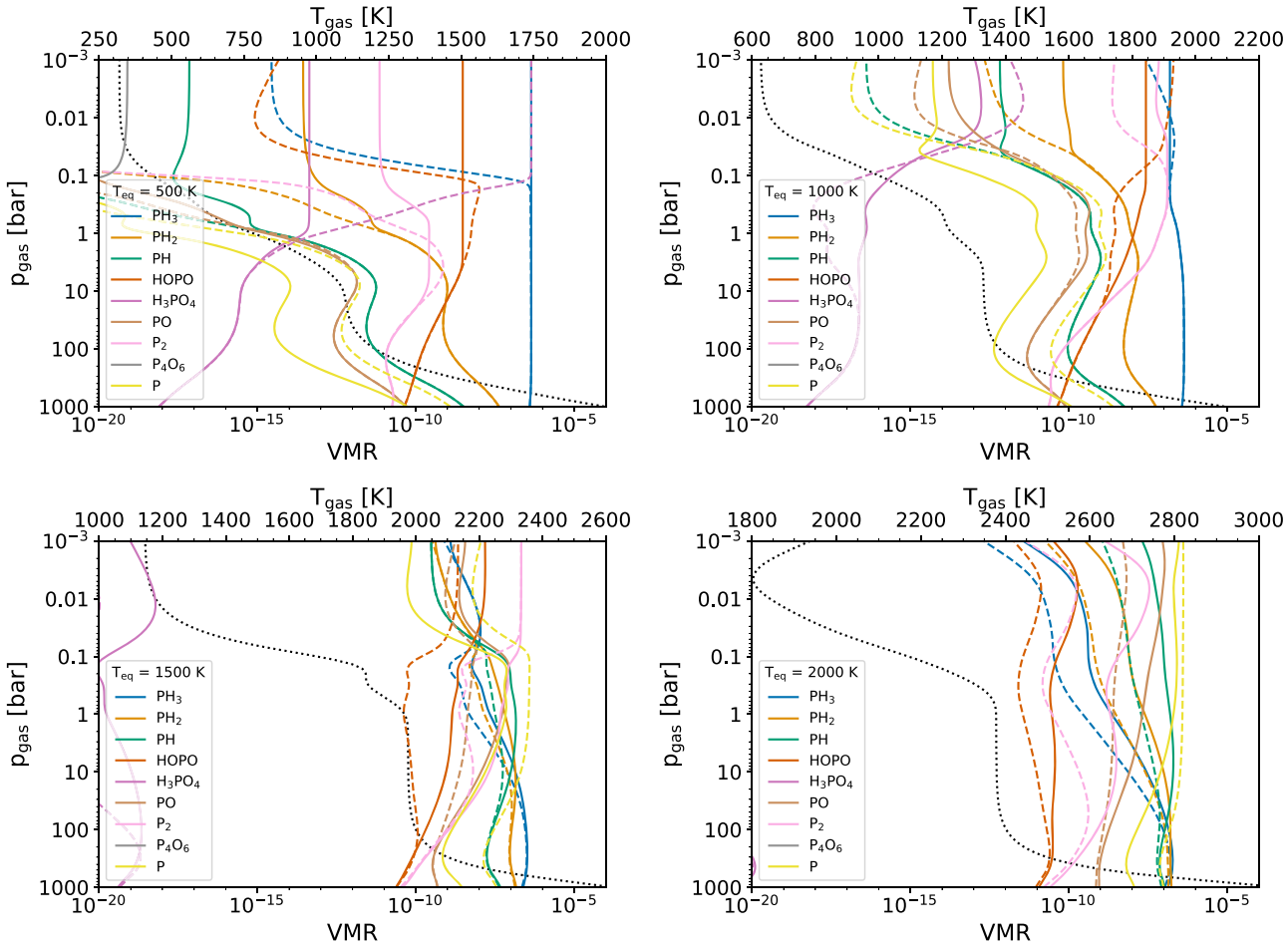

Figure 2. VULCAN PHO network results of VMRs (colored solid lines) for comparison to the D. Wang et al. (2017; their Figure 2) results. The chemical equilibrium volume mixing ratios are denoted by the colored dashed lines. This shows results for various PHO species of interest across the hot Jupiter T–p profiles with equilibrium temperatures $T_{eq} = 500$, 1000, 1500, and 2000 K (black dotted lines; D. Wang et al. 2017). A constant $K_{zz} = 10^9$ cm^2 s^{-1} and solar metallicity is assumed as in D. Wang et al. (2017).

In Figure 3, we compare the $T_{eq} = 500$ K results directly from D. Wang et al. (2017) and the new network. We produce consistent profiles for PH_3 and HOPO, but differences are seen for the other molecules, suggesting the new network generally produces different results from the D. Wang et al. (2017) network. We find larger differences in the upper atmosphere, in particular H_3PO_4 which is different by 4 orders of magnitude between the models. P_2 also shows a large difference, by 4 orders of magnitude in the upper atmosphere. Overall, these results show a relative level of consistency between our study and D. Wang et al. (2017) at least for the major species PH_3 and HOPO, but large differences are seen for the minor species. This suggests that the updated rates in the new network significantly alter the chemical profiles compared to the D. Wang et al. (2017) network.

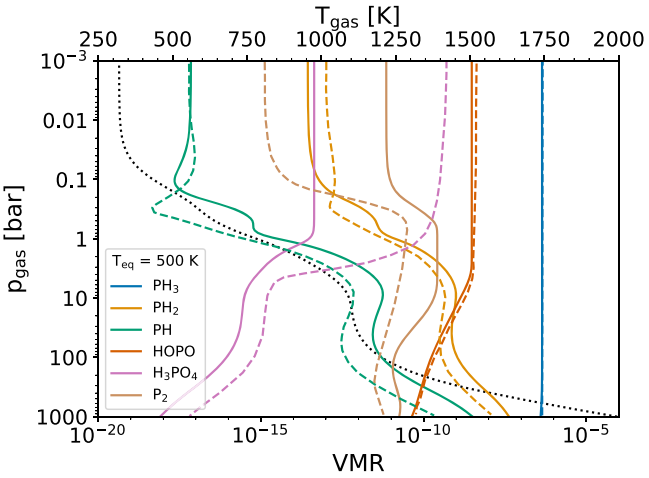

Figure 3. Updated PHO network (solid lines) compared to the results in D. Wang et al. (2017; dashed lines) for the $T_{eq} = 500$ K test case from D. Wang et al. (2017).

4. Application to Hot Jupiter Atmospheres

In this section, we apply the PHO photochemical network to the benchmark hot Jupiter, HD 189733b 1D model parameters presented in J. I. Moses et al. (2011), taking the T–p, K_{zz}, and stellar flux model from that study. We perform a solar and 10 times solar metallicity model for a thermochemistry-only and photochemical test and assess the impact of photochemistry on the vertical profiles of PHO species. Figure 4 shows the input T–p and K_{zz} profile.

Figure 5 presents the results of the model calculations. In the thermochemical-kinetics-only models, our results suggest that at solar metallicity P_2 is the main P carrier at pressure levels less than 1 bar, generally maintaining its equilibrium abundance throughout. PH_3 is generally confined to the deeper atmosphere (>1 bar) and at chemical equilibrium. For 10 times solar, the atmosphere becomes

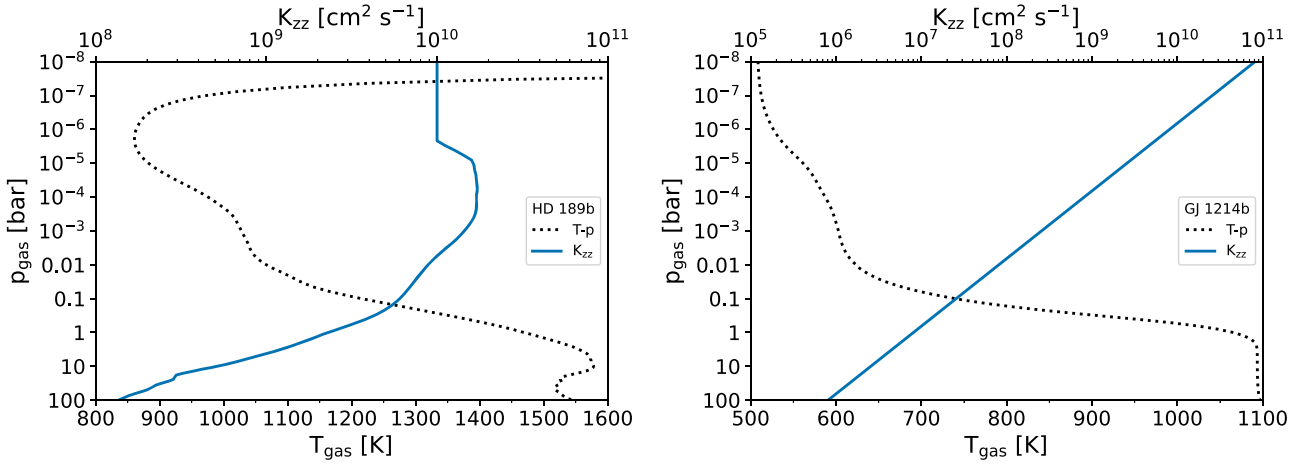

Figure 4. Input T–p and K_{zz} profiles for the HD 189733b case (left) and GJ 1214b case (right) used in this study.

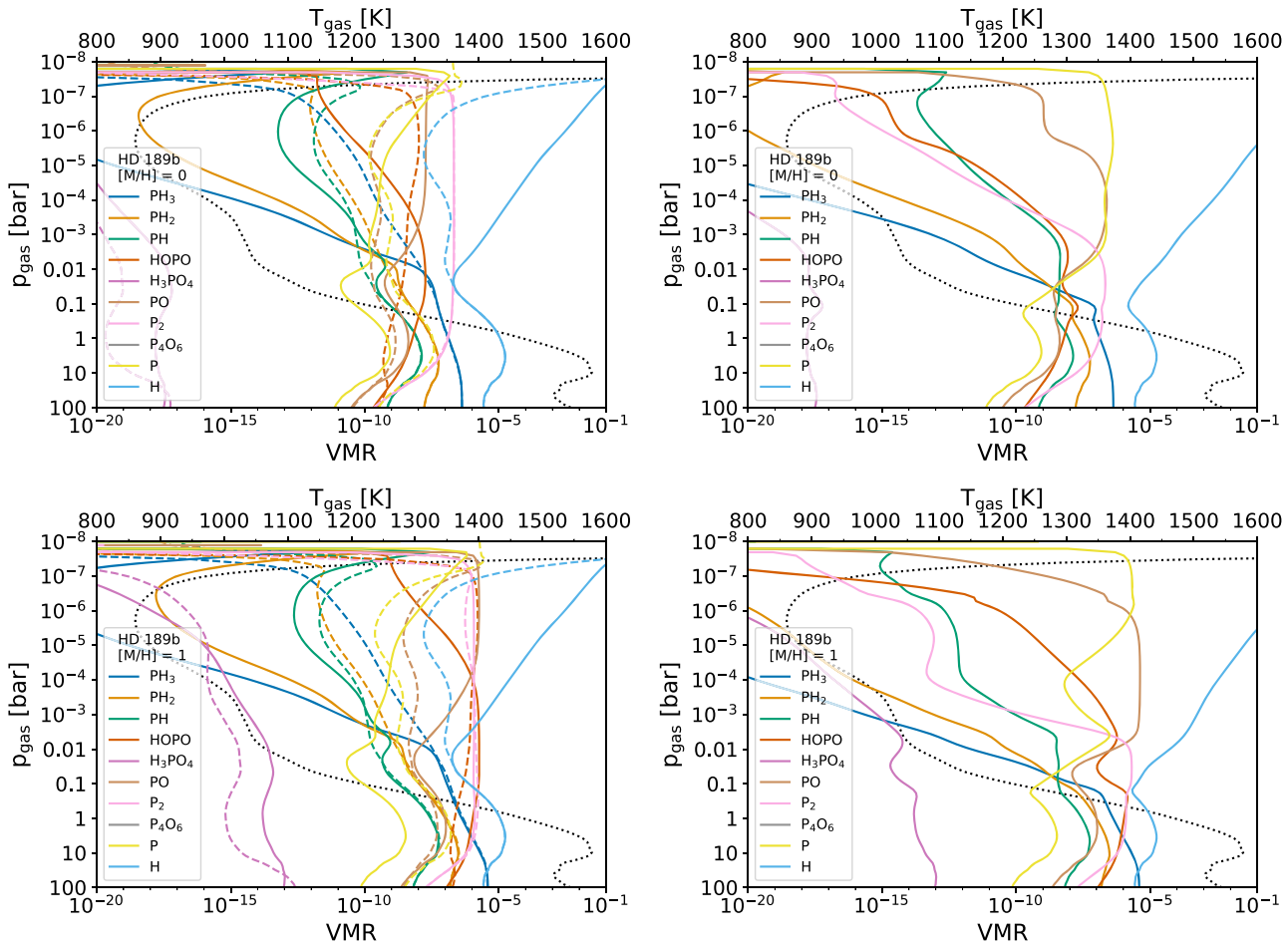

Figure 5. VULCAN PHO network results for the benchmark 1D HD 189733b case. The VMR of each species is shown as solid lines and the T–p profile as a black dotted line. The dashed lines denote the chemical equilibrium values. Top left: thermochemistry only at [M/H] = 0. Top right: photochemical model at [M/H] = 0. Bottom left: thermochemistry only at [M/H] = 1. Bottom right: photochemical model at [M/H] = 1.

more oxygenated, with HOPO, PO, and P_2 dominating the atmospheric composition. Our results indicate a rapid reaction pathway producing HOPO and PO, significantly pushing them and PH_3 out of equilibrium in the upper atmosphere. PH_3 is now confined to a very deep atmosphere at pressures greater than 10 bar.

Comparing the $T_{eq} = 1000$ K from Figure 2 to our HD 189733b thermochemical kinetics only results shows a similar PH_3 profile at high pressure, but the inclusion of the upper atmosphere, different mixing profiles, and T–p profiles affects the P_2 abundance in the HD 189733b case differently to the D. Wang et al. (2017) $T_{eq} = 1000$ K profile.

The impact of photochemistry on PHO chemistry is stark in Figure 5. For both metallicity cases, the larger molecules are photodissociated, leaving P_2 and PO as the P-carrying species in the middle and upper atmosphere. This is because photochemistry directly breaks down or produces radicals (primarily H) that leave

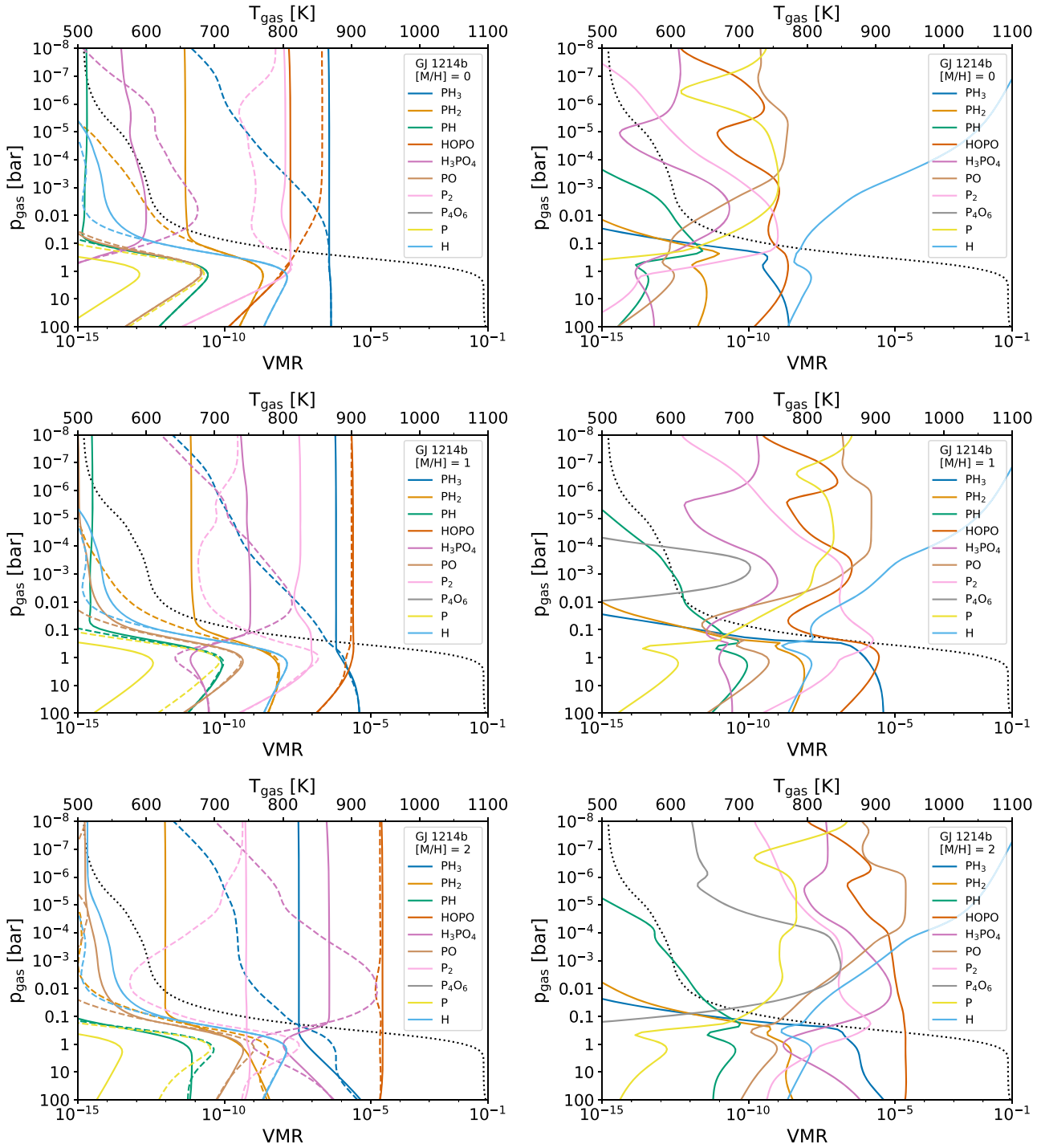

Figure 6. VULCAN PHO network results for the benchmark GJ 1214b 1D case, with the J. I. Moses et al. (2022) K_{zz} expression. The VMR of each species is shown as solid lines and the T–p profile as a black dotted line. The dashed lines show the chemical equilibrium values for each species. Top left: thermochemistry only at [M/H] = 0. Top right: photochemical model at [M/H] = 0. Middle left: thermochemistry only at [M/H] = 1. Middle right: photochemical model at [M/H] = 1. Bottom left: thermochemistry only at [M/H] = 2. Bottom right: photochemical model at [M/H] = 2.

behind only simple, small molecules with relatively strong bonds. PH_3 is severely depleted from the upper atmosphere through photochemical effects, with PH now being the most abundant hydrogen-bearing P molecule, suggesting that photochemistry induces a cascade from PH_3 to PH_2 and PH, also commonly seen for NH_3 and CH_4 photochemistry. For the 10 times solar case, the initial abundances of HOPO and P_2 are reduced by photochemistry leaving a PO-dominated atmosphere, this also suggests radical formation, such as H which is in high abundance in the mid-upper atmosphere, that destroys HOPO (Section 7). We discuss the key chemical pathways that give rise to the results in Section 7 and the potential observational aspects of these results in Section 8.

5. Application to Warm Neptune Atmospheres

In this section, we apply the PHO network to the GJ 1214b system as a representative warm Neptune atmosphere. We

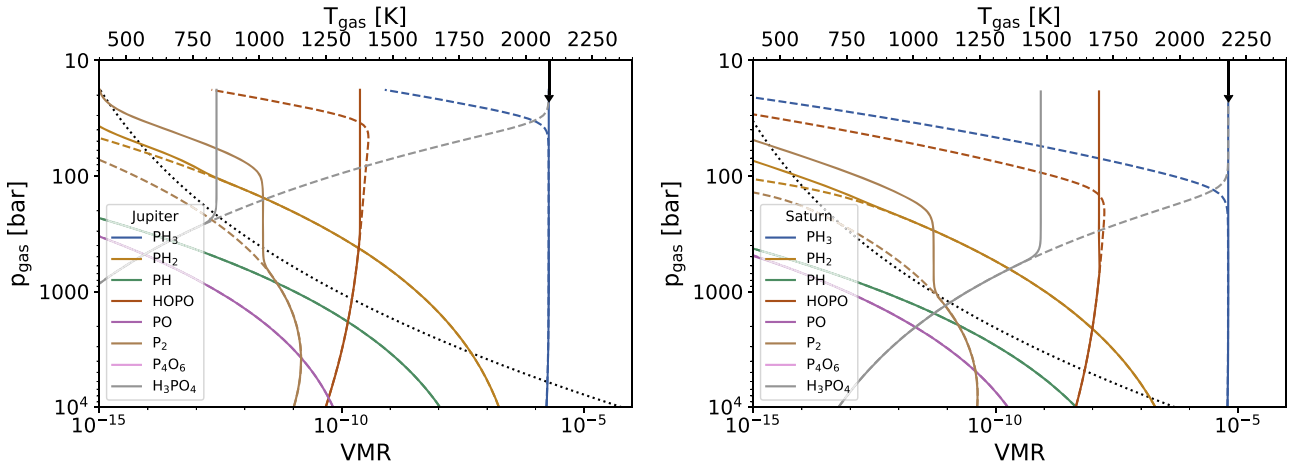

Figure 7. VULCAN PHO network results for the deep Jupiter (left) and Saturn (right) with the T–p profile from J. I. Moses et al. (2005) extended to 10^4 bar assuming an adiabat, and assuming a constant $K_{zz} = 10^8$ cm^2 s^{-1} (D. Wang et al. 2016). The VMR of each species is shown as solid lines and the T–p profile as a black dotted line. The dashed lines denote the chemical equilibrium abundances. The black arrow denotes the PH_3 abundance retrieved by L. N. Fletcher et al. (2009) at lower-pressure regions.

calculate a global average T–p profile for GJ 1214b using the HELIOS radiative–convective equilibrium model (M. Malik et al. 2017), which is then used as input to the VULCAN model. We examine solar, 10 times solar, and 100 times solar metallicity cases and follow the K_{zz} profile expression from the J. I. Moses et al. (2022; their Equation (1)) study, scaled to the properties of GJ 1214b ($H_{1\ mbar} = 209$ km, $T_{eff} = 679$ K). This leads to a K_{zz} profile similar to J. I. Moses et al. (2022)'s Figure 2. $T_{eff} = 700$ K. Figure 4 shows the input T–p and K_{zz} profile.

Figure 6 presents the GJ 1214b test cases. For the thermochemical-kinetics-only cases without photochemistry, PH_3 is dominant only in the solar-metallicity case, while being replaced by HOPO in the higher-metallicity cases. Species are quenched around the 0.1 bar pressure level in all cases, leading to strong nonequilibrium behavior at pressures probed by transmission and emission. The higher abundance of HOPO at chemical equilibrium at higher metallicites along with the quenching behavior, contributes to its ubiquity in the upper atmosphere. For the photochemical cases, as in the HD 189733b case, the effects are striking, again, HOPO, PO, and P_2 tend to dominate most of the upper atmosphere, with PH_3 being confined to its chemical equilibrium abundances in the deep atmosphere. The production of H radicals in the upper atmosphere due to photochemical processes, promotes the destruction of the initial HOPO, leading to a PO-dominated composition. This large H radical production is not present in the nonphotochemical models. We discuss the key chemical pathways that give rise to the results in Section 7 and the potential observational aspects of these results in Section 8.

6. Application to Deep Jupiter and Saturn Atmospheres

In this section, the network is applied to the deep atmospheres of Jupiter and Saturn. We take the T–p profiles for both gas giants from J. I. Moses et al. (2005), following an adiabatic profile to extend it to 10^4 bar, and assume a constant $K_{zz} = 10^8$ cm^2 s^{-1}, following (D. Wang et al. 2016). For Jupiter, we take the P and O abundances from Table 1 in O. Mousis et al. (2021), specifically the O ratio (1450 ppm) from C. Li et al. (2020) and P ratio (1.08 ppm) from L. N. Fletcher et al. (2009). For Saturn, we take the P ratio value from S. K. Atreya et al. (2020; 3.64 ppm) and the O ratio from T. Cavalié et al. (2024), which was estimated to be around 8 times the solar values of K. Lodders (2021; 4100 ppm). We take He ratios for both planets from the S. K. Atreya et al. (2020) review.

In Figure 7, we present the results for the Jupiter and Saturn profiles, which show an interesting dynamic: the initial chemical equilibrium abundance of H_3PO_4 decreases from its initial value, because of dissociation into $HOPO_2$. Eventually, H_3PO_4 becomes a negligible species in both atmospheres. H_3PO_4 is quenched at a pressure level of around 300 bar at these low abundances, which allows PH_3 to form and mix upward to the upper atmosphere from its initial CE abundance to its observed abundance (L. N. Fletcher et al. 2009). P_4O_6 is produced in negligible amounts in both models.

7. Discussion

In this section, we discuss aspects of the PHO network and the main chemical mechanisms that drive our results. In addition, we discuss the shortcomings of the model and gaps in the network that can be expanded and addressed with further experimental and theoretical efforts.

7.1. Oxygenation Mechanisms

In this section, we describe the formation mechanisms of the small oxygenated molecules that are most ubiquitous in the simulations. We focus on the formation of P_2, PO, and HOPO as they are the main products of the network.

7.1.1. Small Oxygenated Phosphorus Species

A key result from our simulations is that small oxygenated phosphorus species play a major role in the phosphorus chemistry in exoplanet atmospheres, in particular HOPO and PO. The only exoplanet simulation where PH_3 is dominant in the upper atmosphere is in the GJ 1214b case without photochemistry. Our results suggest that metal enhancement and photochemistry efficiently produce HOPO, PO, and P_2, which are found in larger abundance than PH_3.

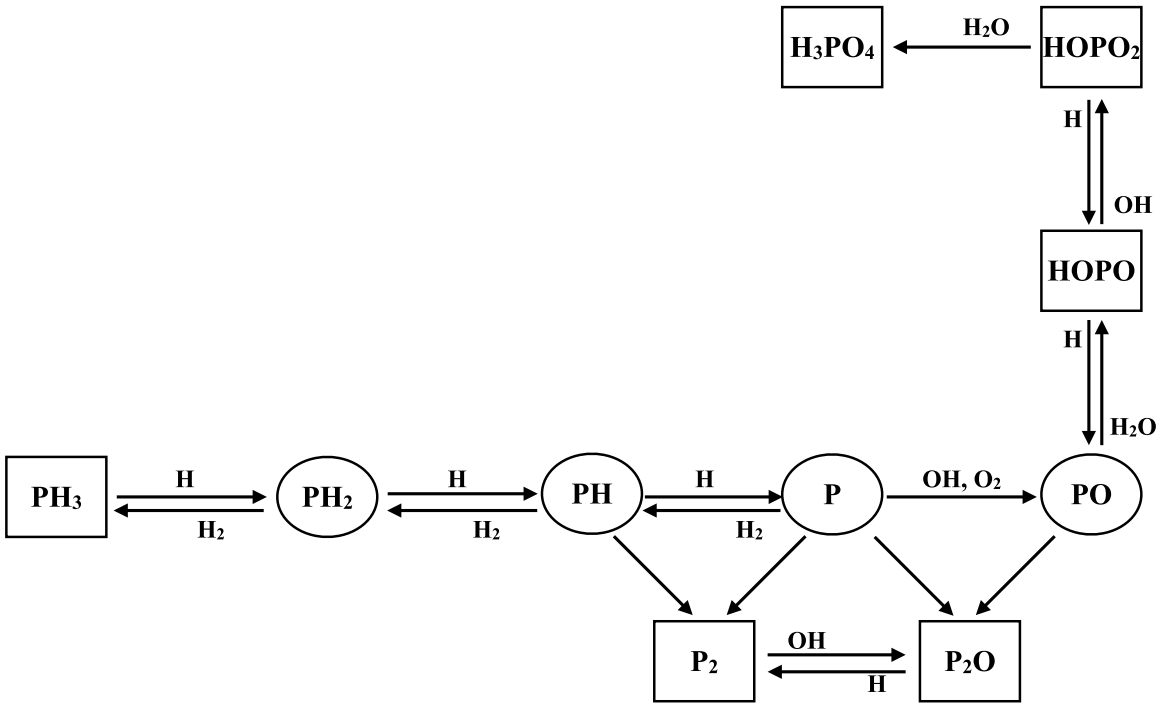

Figure 8. Diagram showing the main chemical pathways present in the PHO scheme between key species.

In the network, the formation of P_2 follows a simple path from PH_3 and subsequent reactions with radicals e.g.,

$$\begin{aligned} 2(PH_3 + H &\rightarrow PH_2 + H_2)\\ 2(PH_2 + H &\rightarrow PH + H_2)\\ PH + H &\rightarrow P + H_2\\ P + PH &\rightarrow P_2 + H\\ 2H_2[M] &\rightarrow 4H\\ \text{net: } 2PH_3 &\rightarrow P_2 + 3H_2. \end{aligned} \quad (1)$$

This pathway enables a rapid formation of P_2 in the atmosphere, especially when photochemistry contributes to the dissociation of hydrogen and produces H radicals, which can further dissociate PH_x molecules through the mechanism in Equation (1). P_2 is also naturally favored at chemical equilibrium in the hot Jupiter HD 189733b models, as shown by the thermochemical model results. In cooler atmospheres that experience low irradiation, such as Jupiter, $PH_2 + PH_2 + M = P_2H_4 + M$ can compete with other loss processes for PH_2, and if P_2H_4 condenses, the phosphorus will be locked into the condensed state.

Formation of PO follows a similar route but with odd-oxygen radicals (OH or O) reacting with P e.g.,

$$\begin{aligned} PH_3 + H &\rightarrow PH_2 + H_2\\ PH_2 + H &\rightarrow PH + H_2\\ PH + H &\rightarrow P + H_2\\ P + OH &\rightarrow PO + H\\ H_2O + H &\rightarrow OH + H_2\\ \text{net: } PH_3 + H_2O + 3H &\rightarrow PO + 4H_2. \end{aligned} \quad (2)$$

The last oxygenation steps are very rapid reactions (K. M. Douglas et al. 2022), allowing efficient formation of PO when odd-oxygen radicals are available in the atmosphere. This is particularly true when photochemistry is occurring, explaining the large amount of PO produced in the photochemical simulations of both hot Jupiters and warm Neptunes.

HOPO forms directly from PO as noted in D. Wang et al. (2016), and with the derived rate from T. M. Jayaweera et al. (2005)

$$PO + H_2O \rightarrow HOPO + H. \quad (3)$$

The consequences of this reaction are seen primarily in the photochemical models, where in the upper atmosphere HOPO is broken down by radicals to produce PO, while in the deeper atmosphere, HOPO is retained. There is generally a transition region between PO and HOPO in the middle atmosphere, where fewer radicals are being produced compared to the upper atmosphere, and some HOPO survives. As PO diffuses downward, it reacts with H_2O, forming HOPO, while as HOPO diffuses upward, it is broken down into PO by radicals. Without radicals to break down HOPO, HOPO remains the primary P-bearing species as seen in our enhanced metallicity thermochemical-kinetics-only simulations. PO remains a minor species in these thermochemical-kinetics-only simulations.

In Figure 8 we present a diagram of the main chemical pathways between key species in the network. This shows the main routes to produce the small oxygenated molecules starting from PH_3. These follow similar pathways to those in D. Wang et al. (2016).

Overall, the network characteristics show a simple and direct path of conversion of PH_3 to P_2, HOPO, and PO for the solar metallicity models, especially when photochemical processing occurs. At higher metallicities, the balance between HOPO and PO is key to understanding the chemical profile, with photochemical processing playing a major role in determining the transition zones between the two molecules. Without photochemistry, HOPO remains the dominant molecule in these atmospheres.

7.1.2. Formation of H_3PO_4

Formation of the end product H_3PO_4 is driven by the reaction from K. M. Douglas et al. (2022; $HOPO_2 + H_2O + M \rightarrow H_3PO_4 + M$), making the abundance of H_3PO_4 highly dependent

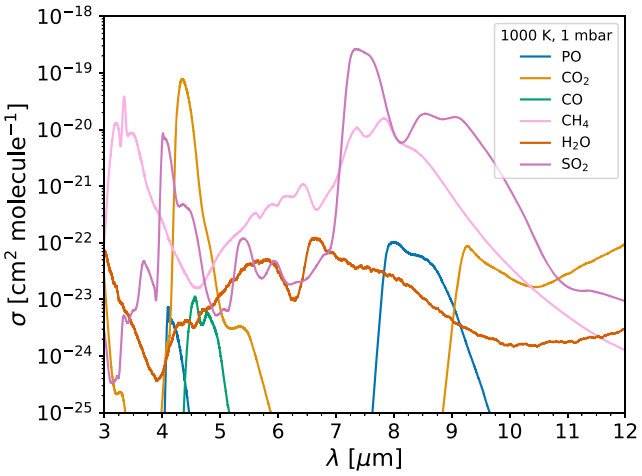

Figure 9. Cross sections of PO, CO_2, CO, CH_4, H_2O, and SO_2 at 1000 K and 1 mbar. Features are seen at around 4.1 and 8 μm, which lie in the wavelength range of NIRSpec, NIRCam, and MIRI JWST instruments, commonly used for exoplanet atmosphere characterization. However, these may be obscured by CH_4 and SO_2.

on the local $HOPO_2$ and H_2O availability. In all thermochemical models, H_3PO_4 remains a minor species except for the cool, metal-enriched systems such as the GJ 1214b 100 times solar model. This suggests H_3PO_4 is only present in metal-enriched scenarios, where the oxygenation process can provide the HOPO and then $HOPO_2$ needed to produce H_3PO_4 This is further evidenced by the GJ 1214b 100 times solar photochemical model, where H_3PO_4 occurs at moderate abundance in the mid atmosphere. This suggests an efficient formation pathway to the end product H_3PO_4 when local thermochemical conditions are suitable. The formation of $HOPO_2$ is primarily driven by the reaction of oxygen radicals with HOPO and other oxygenated phosphorus oxides such as PO and PO_2; these species are produced in generally higher quantities through photochemical processing, especially at high metallicity.

We caution that we have not included any other pathways for the formation and destruction of H_3PO_4, and as noted in Section 6, we lack high-pressure rate data for the reaction involving H_3PO_4, which could level off the rate of formation of this molecule at moderate to high pressures.

7.1.3. Formation of P_4O_6

Our results suggest the formation of the P_4O_6 end product is highly unfavorable in all thermochemical environments. It occurs maximally at the parts-per-billion level in highly metal-enriched and photochemical environments. However, we again caution that we have only explored a single P_4O_6 formation pathway.

7.2. Data Gaps and Needs

In this section, we discuss the current gaps in the PHO network and potential areas of improvement. Several general areas of uncertainty remain for the kinetics of P chemistry are listed below.

1. Many rate coefficients are theoretical estimates. While simple recombination reactions can probably be calculated reasonably accurately (within a factor of 2), reactions over complex potential energy surfaces involving barriers are much more uncertain.
2. Sources and derivations of rate data are not fully consistent across the species list.

More specifically, we highlight below reactions with significant sensitivity in the model, where improved estimates of rate coefficients would be particularly beneficial, as well as additional reaction pathways.

1. Reactions that build P_4 (e.g., $P_2 + P_2 + M$).
2. Reactions that build P_2H_2 and P_2H_4 (e.g., $PH + PH + M$ and $PH_2 + PH_2 + M$), which are both molecules of atmospheric interest, especially in cold-reducing environments.
3. Bimolecular reactions involving radicals interacting with phosphorus oxides such as PO, PO_2, and PO_3.
4. Additional pathways for building larger oxidized molecules such as H_3PO_4 and P_3O_4.
5. Several high-pressure rates are unknown for important combination reactions such as $OH + PO + M \rightarrow HOPO + M$.
6. We lack the high-pressure rate for the reaction that forms H_3PO_4.

On the photochemistry side, several aspects of data are missing or incomplete.

1. Photodissociation of larger molecules such as H_3PO_4 is not included.
2. Only one photolysis product branch is given for each phosphorus molecule with unknown quantum efficiencies.

Overall, the PHO network remains highly approximate, with many reactions containing uncertain and estimated rates. Significant effort will be required to experimentally and theoretically build a more reliable and sound PHO network; however, our current study provides a useful guide into what mechanisms require the most attention going forward.

7.3. Combining with the SNCOH Network

In this study, we have focused on the PHO system exclusively, ignoring the impact of S, N, and C species on the P chemistry, which may be significant. However, our PHO-only effort allows us to analyze the main properties and mechanisms of the proposed PHO photochemical scheme without interference from other species. Several additions will have to be made to properly integrate the scheme into the SNCOH network. Of note, two important molecules and their pathways in the full SNCOHP network are PS and PN, where some reaction rates of PN species are available in K. M. Douglas et al. (2022). These aspects will be explored in a follow-up paper.

We can expect several effects on the P species from adding S, N, and C species. For example, the addition of SNCOH will affect the impact of photochemistry on P species through increased UV shielding. This would reduce the effectiveness and depth that photolysis of P products occurs, possibly changing the vertical profiles of P species. In particular, the boundary between HOPO and PO may change due to this effect, as changes in the H radical vertical profile occur with the addition of other species.

Reactions with S, N, and C radicals with P species will produce PN, PS, and CP complexes, possibly reducing the amount of HOPO and PO seen in the simulations with the PHO-only network. In addition, more H radicals may be present at deeper depths when additional molecules such as NH_3 and H_2S are included, greatly affecting the chemical structure of the atmosphere. This may reduce the HOPO and PO to below parts-per-million levels, making it harder to detect in these atmospheres. Overall though, we expect similar P

species (HOPO, PO, and P_2) to be produced with the full network, and our main conclusions regarding the chemical mechanisms should not be significantly affected.

8. Observational Consequences

Our results suggest that for hot Jupiters like HD 189733b, PH_3 will not be detectable in both transmission and emission with current instrumentation, because PH_3 remains below the parts-per-million level at pressure levels probed by transmission and emission ($\sim$1–10^{-4} bar). Only in the deep atmosphere does the PH_3 abundance rise above the parts-per-million level. We find photochemical processing creates a large PO abundance, especially at enhanced metallicities. This makes PO a promising molecule to detect with JWST and other telescopes.

For warm Neptunes like GJ 1214b, a similar picture emerges, where HOPO and PO remain the strongest P-bearing species to detect, especially at higher metallicities and with photochemical processing. P_2 is a homonuclear molecule and probably does not have strong absorption features. Atomic P appears in the very upper atmosphere in some cases, but this only has strong lines at UV wavelengths (e.g., R. L. Kurucz & B. Bell 1995). Our results suggest PH_3 will also not be detectable in transmission or emission for this class of planet.

Overall, our study suggests that the P-bearing species of interest for exoplanet characterization are HOPO and PO, of which only PO currently has line-list data (L. Prajapat et al. 2017). In Figure 9, we present cross sections of PO produced using the L. Prajapat et al. (2017) line-list data at 1000 K and 1 mbar, compared to other molecules of interest found in hot Jupiter and warm Neptune exoplanets. These show features in bands at around 4.1 and 8 μm, which are probed by the commonly used NIRSpec G395H, NIRCam Grism, and MIRI Low-Resolution Spectrometer JWST modes, suggesting that observational evidence for PO may already be present in current JWST data for metal-enhanced planets. However, the 4.1 μm PO band would be obscured by the presence of SO_2, CH_4 as well as CO_2, which have much larger cross sections in that wavelength range. PO may fill in the gap between the SO_2 feature and the ramp in the opacity of the CO_2 feature, leading to an apparent steeper climb in opacity near 4.1 μm compared to just SO_2 and CO_2 alone. A promising distinguishing feature is the 8μm band for PO, which would be clearly apparent above the H_2O opacity and fill in the gap between the SO_2 bands and appear to broaden the 7.5 μm SO_2 feature. If CH_4 is present, it is likely to dwarf any PO signal in these JWST wavelength ranges.

The formation of SO_2 is favored at metallicities around 10 times solar (S.-M. Tsai et al. 2023), which is also the range where the PHO network produces PO at parts-per-million levels. This suggests SO_2 and PO may form together as photochemical products in this range for hot Jupiters and warm Neptunes.

9. Summary and Conclusions

In this study, we present a PHO photochemical network for exoplanet atmospheres by updating the D. Wang et al. (2016) PHO network with new reaction rates sourced from the literature and with new theoretical calculations. We also add 10 photochemical reactions that impact P-bearing species, some with new theoretical UV cross sections. Overall, we were able to update around 25% of the D. Wang et al. (2016) network, improving the robustness of the overall network substantially. For the first time, we explored a P_4O_6 formation mechanism by calculating theoretical rates for the termolecular recombination reaction ($P_2O_3 + P_2O_3 + M \rightarrow P_4O_6 + M$) but found the P_4O_6 abundance to be a negligible component in the atmospheres simulated.

Overall, our results suggest that for hot Jupiters and warm Neptunes, HOPO, PO, P_2, and atomic P are the key P-bearing species, especially at higher metallicities and where photochemical processing is present. Our results suggest PH_3 is only seen in solar metallicity, cold planets where photochemistry is negligible, as well as cold planets with similar O and P ratios to Jupiter and Saturn. We suggest that retrieval models include PO as part of their species detection suite and include HOPO when line lists or opacity data become available. Due to the spectral features of PO, this molecule may already be traceable in current JWST NIRSpec, NIRCam, and MIRI transmission and emission spectra data of metal-enhanced planets.

Despite our progress, we caution that our proposed PHO network contains many approximate rate coefficients and potentially missing key reaction pathways, and so strong conclusions regarding the abundance predictions from these simulations should be considered carefully. These concerns will need to be addressed through future experiments and theoretical calculations to put phosphorus kinetics on a firmer footing.

Our study points to the importance of considering photochemistry for P networks and provides physical mechanisms for consideration when interpreting observational data for PH_3 (non)detection. Due to PH_3's status as a biomarker molecule, improving the accuracy of phosphorus kinetic networks through experimental and/or theoretical efforts will be an important goal for the exoplanet field going into the near future. Our PHO study forms the basis for our future combined PSCHNO photochemical network.

Acknowledgments

E.K.H.L. is supported by the SNSF Ambizione Fellowship grant (No. 193448). S-M.T. is supported by the University of California at Riverside. J.M.C.P. was supported by the UK Science and Technology Facilities Council (grant ST/P000517/1). J.M. and C.V. were supported by NASA Exoplanet Research Program grant 80NSSC22K0314. This material is based in part on work supported by the U.S. Department of Energy, Office of Science, Office of Basic Energy Sciences, Division of Chemical Sciences, Geosciences, and Biosciences under contract No. DE-AC02-06CH11357. We thank P. Rimmer for advice on the ARGO Venus phosphorus photochemical model.

Software: VULCAN (S.-M. Tsai et al. 2017, 2021)

Appendix A
Theoretical Contributions to the PHO Network

A.1. Theoretical Kinetics Calculation for PxHy Reactions

Ab initio transition state theory (TST) was used to predict the rate constants for the abstractions $^3PH + H \rightarrow {}^4P + H_2$; $^2PH_2 + H \rightarrow {}^3PH + H_2$; $PH_3 + H \rightarrow {}^2PH_2 + H_2$; and $^3PH + {}^2PH_2 \rightarrow {}^4P + PH_3$. The rovibrational properties of the stationary points on these potential energy surfaces were evaluated at the CCSD(T)/cc-pV(Q+D)Z level. The barrier heights were evaluated with a composite approach that combined (i) a CCSD(T) complete basis set (CBS) limit obtained from extrapolation of cc-pV(5+D)Z and cc-pV(6+D)Z energies, (ii) CCSDT(Q)/cc-pV(D+D)Z corrections for higher-order

Table 2
Molecular Properties of the Stationary Points on the Potential Energy Surfaces for PO + OPO and P_2O_3 + P_2O_3 and Some Relevant P_xH_y Species

Molecule	Geometry (CartesianCo-ordinates in Å)[a]	Rotational Constants (GHz)[a]	Vibrational Frequencies (cm^{-1})[a]	$\Delta_f H°$ (298 K) (kJ mol^{-1})[b]	$\Delta_f G°$ (298 K) (kJ mol^{-1})[b]
PO	P 0.0 0.0 0.0585 O 0.0 0.0 1.5415	21.78804	1240	−41.14	−63.36
PO_2	P 0.087 0.0 0.041 O 0.032 0.0 1.5156 O 1.182 0.0-0.949	97.5896 8.54002 7.85283	382 1059 1304	−286.2	−288.9
P_2O_3	P 1.301-0.306-0.456 P -1.633 0.378 0.039 O 2.472 0.337 0.147 O -0.024 0.692-0.168 O -1.843-1.044 0.347	12.5877 1.70504 1.56174	34 101 132 329 442 609 784 1256 1279	−644.5	−630.4
P_4O_6	O -1.537 0.935 0.209 O -2.835-1.257 0.219 O -0.291-1.284 0.070 O -1.451-2.068 2.200 O -0.151 0.124 2.190 O -2.696 0.150 2.339 P 0.014-1.457 1.697 P -2.951-1.427 1.872 P -1.599-0.512-0.611 P -1.437 1.129 1.860	1.04977 1.04977 1.04977	267 (×3) 294 (×2) 388 (×3) 533 (×3) 564 (×3) 588 621 (×3) 640 (×2) 712 908 (×3)	−1659	−1531
PH	P 0.0 0.0 0.086 H 0.0 0.0 1.514	254.08252	2347	238.2	211.4
PH_2	P 0.0 0.115 0.0 H 1.021-0.876 0.0 H -1.0214-0.876 0.0	271.85867 240.33917 127.56455	1130 2365 2373	138.6	124.5
P_2H_2	P 0.450 1.229 1.470 H 0.139 0.635 2.716 P -0.207-0.323 0.354 H 0.153 0.269-0.891	129.19206 7.53928 7.12357	613 694 780 979 2333 2349	124.6	113.7
P_2H_4	P -0.361 0.249-1.097 H -0.277-1.101-1.518 P -0.361-0.249 1.097 H 1.022-0.491 1.287 H 1.022 0.491-1.287 H -0.277 1.101 1.518	65.47798 5.67029 5.65539	198 418 630 653 815 885 1119 1126 2377 2387 2393 2401	37.98	60.18
P_2	P -2.086 0.682 0.0 P -0.195 0.812 0.0	9.088113	800	145.3	104.8

Notes.
[a] Calculated at the B3LYP/6-311+g(2dp) level of theory.
[b] Enthalpy and Gibbs free energy of formation at 298 K calculated at the G4 level of theory and using reference values for P(*g*) and H(*g*) of $\Delta_f H°$ (298 K) = 316.39 and 218.00 kJ mol^{-1}, respectively (M. Chase 1998).

excitations, (iii) and CCSD(T)/CBS core-valence corrections from all electron calculations for TZ and QZ basis sets. The partition functions were evaluated within the rigid-rotor harmonic oscillator approximation. Asymmetric Eckart tunneling corrections were also included.

The radical-radical recombination of PH_2 with PH_2 was treated with variable reaction coordinate (VRC)–TST. A direct sampling CASPT2/cc-pV(T+D)Z approach was used to evaluate the interaction energies in the transition state region. One-dimensional P–P distance-dependent corrections were obtained from the combination of a geometry relaxation correction and a complete basis set limit correction. The geometry relaxation correction was obtained from constrained geometry evaluations at the CASPT2/cc-pV(Q+D)Z level. The basis set relaxation correction was obtained from extrapolation of CASPT2/cc-pV(5+D)Z and CASPT2/cc-pV(6+D)Z evaluations along the CASPT2/cc-pV(Q+D)Z minimum energy path. A dynamical correction of 0.85 was applied to the final VRC–TST predictions.

Pressure-dependent predictions for the $^2PH_2 + {}^2PH_2 \rightarrow P_2H_4 \rightarrow PPH_2 + H_2$ system were obtained from one-dimensional master equation simulations incorporating the VRC–TST flux for the recombination channel. The remaining channels were treated as described above for the abstraction reactions. One-dimensional hindered rotors were included as appropriate. The energy transfer rates were treated within the exponential down formalism and Lennard–Jones collision rates.

The PH + H and PH_2 + H recombination reactions were similarly treated with VRC–TST, but now employing multi-reference configuration interaction MRCI+Q based evaluations for the direct sampling over the interaction potential. These direct evaluations included the Davidson correction for higher-order interactions and were performed for the aug-cc-pV(T+D)Z basis. A dynamical correction of 0.9 was applied to the final VRC–TST predictions. One-dimensional master equation simulations were again used to predict the pressure dependence, with the binding energies determined from equivalent CCSD(T)-based composite methods.

A.2. Theoretical Calculations of Cross Sections and PxOyHz Rate Constants

Electronic structure calculations were carried out using the Gaussian 16 suite of programs (M. J. Frisch et al. 2016). Vibrational frequencies, rotational constants, and energies were calculated at the B3LYP/6-311+g(2d,p) level of theory, and energies using the very accurate G4 fourth-generation compound method of L. A. Curtiss et al. (2007). The Cartesian coordinates, molecular parameters, enthalpies, and free energies of formation of the relevant phosphorus oxides and hydrides are listed in Table 2. Their molecular geometries are illustrated in Figure 10.

To calculate photodissociation spectra for PO, PO_2, P_2, P_2H_2, and P_2H_4, their geometries were first optimized at the B3LYP/6-311+g(2d,p) level of theory (M. J. Frisch et al. 2016). Vertical excitation energies and transition dipole moments for transitions from the ground state of each molecule to the first 30 electronically excited states were then calculated using time-dependent density function theory (TD-DFT; R. Bauernschmitt & R. Ahlrichs 1996). P_2H_2 and P_2H_4 both photolyze at longer wavelengths by cleavage of the P–P bond, yielding PH + PH or PH_2 + PH_2 with photolysis thresholds of 338 nm and 508 nm, respectively (these thresholds correspond to the energy required to break the P–P bond). In the case of P_2, the photolysis threshold is 247 nm. Rate coefficients for the

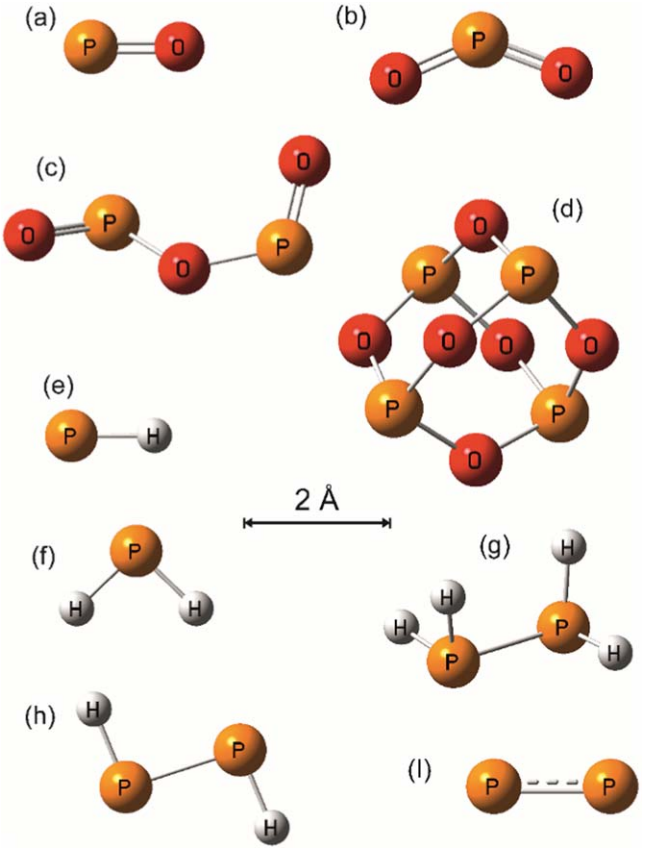

Figure 10. Molecular geometries of (a) PO, (b) PO_2, (c) P_2O_3, (d) P_4O_6, (e) PH, (f) PH_2, (g) P_2H_4, (h) P_2H_2, and (i) P_2.

recombination reactions $PO + PO_2 \rightarrow P_2O_3$ and $P_2O_3 + P_2O_3 \rightarrow P_4O_6$ were calculated using the Master Equation Solver for Multi-Energy well Reactions program (D. R. Glowacki et al. 2012). The internal energy of each species on the potential energy surface was divided into a contiguous set of grains (width 150 cm^{-1}) containing a bundle of rovibrational states, where the density of states was calculated using the relevant data in Table 2. Each grain was then assigned a set of microcanonical rate coefficients for dissociation back to the reactants ($PO + PO_2$, or $P_2O_3 + P_2O_3$) using an inverse Laplace transformation to link them directly to the high-pressure limiting recombination coefficients (k_∞). These coefficients were estimated using long-range transition rate theory (Y. Georgievskii & S. J. Klippenstein 2005) to be $k_\infty(PO + PO_2) = 7.3\ 10^{-10}\ (T/298)^{0.167}\ cm^3\ molecule^{-1}\ s^{-1}$ and $k_\infty(P_2O_3 + P_2O_3) = 8.4\ 10^{-10}\ (T/298)^{0.167}\ cm^3\ molecule^{-1}\ s^{-1}$. The exponential down model was used to estimate the probability of collisional transfer between grains. The calculations were performed with N_2 as the third body, where the average energy for downward transitions was set to $\langle \Delta E_{down} \rangle = 300\ (T/298)^{0.25}\ cm^{-1}$ (R. Gilbert & S. Smith 1990). The second-order recombination rates for the two reactions were calculated over large ranges of temperature (150–500 K) and pressure (10^{-5}–10^4 torr). The low-pressure limiting rate coefficient for $PO + PO_2$ is then $k_0 = 4.56\ 10^{-26}\ (T/298)^{-4.25}\ cm^6\ molecule^{-2}\ s^{-1}$, with a broadening factor $F_c = 0.2$. For $P_2O_3 + P_2O_3$, $k_0 = 2.37\ 10^{-25}\ (T/298)^{-2.99}\ cm^6\ molecule^{-2}\ s^{-1}$, with a broadening factor $F_c = 0.36$.

Appendix B
PHO Reaction Rate List

In the following tables (Tables 3 and 4), we detail the included reactions inside the PHO network. The photochemical reactions are detailed in Section 2.2. References for each reaction are indexed as follows: [a]T. M. Jayaweera et al. (2005), [b]K. M. Douglas et al. (2019, 2020, 2022), [c]A. Twarowski (1995), D. Wang et al. (2016), [d]J. C. Mackie et al. (2002), N. L. Haworth et al. (2002), [e]J. M. C. Plane et al. (2021), [f]D. F. Nava & L. J. Stief (1989), [g]B. K. Fritz et al. (1982), [h]L. Baptista & A. A. de Almeida (2023), [i]This study, [j]J.-C. Lizardo-Huerta et al. (2021).

The coefficients follow the VULCAN formatting and units (S.-M. Tsai et al. 2017, 2021), where the generalized Arrhenius equation is used

$$k = AT^{b}\exp\left(-\frac{E}{T}\right), \tag{B1}$$

where k is the rate coefficient in units of $cm^3\,s^{-1}$ for bimolecular reactions and $cm^6\,s^{-1}$ for termolecular reactions. We follow a convention where odd numbers are the forward reactions and even numbers are the reverse reactions.

Table 3
Updated PHO Reaction Network for the Bimolecular Reactions

Reaction number	Forward reaction (2-body)	A	n	E
R1	$O + OH \rightarrow O_2 + H$	7.47e-10	−0.5	30.0
R3	$OH + H_2 \rightarrow H_2O + H$	3.57e-16	1.52	1740.0
R5	$O + H_2O \rightarrow OH + OH$	8.2e-14	0.95	8570.0
R7	$O + H_2 \rightarrow OH + H$	8.52e-20	2.67	3160.0
R9	$O_1 + H_2 \rightarrow OH + H$	2.87e-10	0.0	0.0
R11	$O_1 + O_2 \rightarrow O + O_2$	3.2e-11	0.0	−70.0
R13	$O_1 + H_2O \rightarrow OH + OH$	1.62e-10	0.0	−65.0
R15	$HO_2 + H \rightarrow OH + OH$	2.81e-10	0.0	440.0
R17	$HO_2 + H \rightarrow O_2 + H_2$	7.11e-11	0.0	710.0
R19	$O + HO_2 \rightarrow OH + O_2$	2.7e-11	0.0	−224.0
R21	$OH + HO_2 \rightarrow H_2O + O_2$	2.4e-08	−1.0	0.0
R23	$H_2O_2 + H \rightarrow H_2 + HO_2$	2.81e-12	0.0	1890.0
R25	$H_2O_2 + H \rightarrow OH + H_2O$	1.69e-11	0.0	1800.0
R27	$O + H_2O_2 \rightarrow OH + HO_2$	1.4e-12	0.0	2000.0
R29	$OH + H_2O_2 \rightarrow H_2O + HO_2$	2.9e-12	0.0	160.0
R31[a]	$OH + HOPO_2 \rightarrow PO_3 + H_2O$	1.993e-18	2.0	1007.0
R33[a]	$H_2 + PO_3 \rightarrow H + HOPO_2$	3.321e-12	0.0	0.0
R35[b]	$O_2 + PO \rightarrow O + PO_2$	2.3e-11	0.0	100.0
R37[b]	$O_2 + P \rightarrow O + PO$	4.2e-12	0.0	600.0
R39[c]	$O_2 + PH \rightarrow O + HPO$	5.25e-13	0.0	2012.16
R41[a]	$H + HOPO \rightarrow H_2O + PO$	4.98e-12	0.0	4176.72
R43[d]	$H + HOPO \rightarrow H_2 + PO_2$	3.55e-17	1.94	5072.45
R45[d]	$H + HOPO_2 \rightarrow H_2O + PO_2$	1.78e-11	0.176	5937.99
R47[a]	$O + HOPO \rightarrow H + PO_3$	1.66e-12	0.0	7548.29
R49[e]	$H + PO_3 \rightarrow OH + PO_2$	1.16e-11	0.5	0.0
R51[c]	$H + P_2O_3 \rightarrow PO + HOPO$	5.25e-11	0.0	6013.62
R53[a]	$H + HPO \rightarrow H_2 + PO$	4e-16	1.5	0.0
R55[i]	$H + PH_3 \rightarrow H_2 + PH_2$	7e-18	2.3576	45.123
R57[i]	$H + PH_2 \rightarrow H_2 + PH$	1.94e-16	1.8025	47.26
R59[i]	$H + PH \rightarrow P + H_2$	1.54e-15	1.5073	5.7185
R61[c]	$H + P_2O \rightarrow OH + P_2$	5.25e-11	0.0	2807.16
R63[c]	$H + P_2O \rightarrow PO + PH$	5.25e-11	0.0	2810.76
R65[c]	$H + P_2O \rightarrow HPO + P$	5.25e-11	0.0	6013.62
R67[c]	$H + P_2O_2 \rightarrow PO + HPO$	5.25e-11	0.0	6013.62
R69[c]	$H + H_2POH \rightarrow H_2O + PH_2$	5.25e-11	0.0	6013.62
R71[c]	$H + H_2POH \rightarrow H_2 + HPOH$	5.25e-11	0.0	2089.13
R73[c]	$H + HPOH \rightarrow H_2O + PH$	5.25e-11	0.0	0.0
R75[c]	$H + HPOH \rightarrow H_2 + HPO$	5.25e-11	0.0	2863.68
R77[a]	$O + HOPO \rightarrow OH + PO_2$	1.66e-11	0.0	0.0
R79[c]	$O + HOPO_2 \rightarrow O_2 + HOPO$	5.25e-11	0.0	4150.6
R81[e]	$O + PO_3 \rightarrow O_2 + PO_2$	5.04e-11	−0.04	0.0
R83[c]	$O + P_2O_3 \rightarrow PO + PO_3$	5.25e-11	0.0	6013.62
R85[c]	$O + P_2O_3 \rightarrow PO_2 + PO_2$	5.25e-11	0.0	6013.62
R87[a]	$O + HPO \rightarrow H + PO_2$	1.66e-11	0.0	1511.0
R89[a]	$O + HPO \rightarrow OH + PO$	2.823e-16	1.5	0.0
R91[c]	$O + P_2 \rightarrow PO + P$	5.25e-11	0.0	2288.78
R93[c]	$O + PH_3 \rightarrow OH + PH_2$	2.855e-18	2.296	915.6
R95[f]	$O + PH_3 \rightarrow HPOH + H$	4.75e-11	0.0	0.0
R97[c]	$O + PH_2 \rightarrow H + HPO$	5.25e-11	0.0	0.0
R99[c]	$O + PH_2 \rightarrow OH + PH$	5.25e-11	0.0	1864.22

Table 3
(Continued)

Reaction number	Forward reaction (2-body)	A	n	E
R101[b]	$O + PH \rightarrow PO + H$	2e-10	0.0	0.0
R103[c]	$O + PH \rightarrow OH + P$	5.25e-11	0.0	1873.84
R105[c]	$O + P_2O \rightarrow O_2 + P_2$	5.25e-11	0.0	1704.26
R107[c]	$O + P_2O \rightarrow PO + PO$	5.25e-11	0.0	849.12
R109[c]	$O + P_2O \rightarrow PO_2 + P$	5.25e-11	0.0	6013.62
R111[c]	$O + P_2O_2 \rightarrow O_2 + P_2O$	5.25e-11	0.0	3089.8
R113[c]	$O + P_2O_2 \rightarrow PO + PO_2$	5.25e-11	0.0	6013.62
R115[c]	$O + H_2POH \rightarrow OH + HPOH$	5.25e-11	0.0	1408.39
R117[c]	$O + HPOH \rightarrow H + HOPO$	5.25e-11	0.0	0.0
R119[c]	$O + HPOH \rightarrow OH + HPO$	5.25e-11	0.0	2310.43
R121[b]	$OH + PO \rightarrow H + PO_2$	1.2e-10	0.0	0.0
R123[d]	$OH + HOPO \rightarrow H_2O + PO_2$	6.17e-11	−0.219	1610.3
R125[e]	$OH + HOPO \rightarrow H + HOPO_2$	7.69e-08	−1.25	0.0
R127[a]	$O + HOPO_2 \rightarrow OH + PO_3$	1.66e-11	0.0	6194.0
R129[c]	$OH + P_2O_3 \rightarrow PO + HOPO_2$	5.25e-13	0.0	6013.62
R131[c]	$OH + P_2O_3 \rightarrow PO_2 + HOPO$	5.25e-13	0.0	6013.62
R133[a]	$OH + HPO \rightarrow H_2O + PO$	2e-18	2.0	1007.0
R135[c]	$OH + HPO \rightarrow H + HOPO$	5.25e-13	0.0	6013.62
R137[b]	$OH + P \rightarrow H + PO$	3.61e-11	−0.29	0.0
R139[g]	$OH + PH_3 \rightarrow H_2O + PH_2$	2.71e-11	0.0	155.15
R141[c]	$OH + PH_3 \rightarrow H + H_2POH$	5.25e-13	0.0	6013.62
R143[c]	$OH + PH_2 \rightarrow H_2O + PH$	5.25e-13	0.0	1126.95
R145[c]	$OH + PH_2 \rightarrow H + HPOH$	5.25e-13	0.0	0.0
R147[b]	$OH + PH \rightarrow H_2O + P$	3.86e-11	0.167	0.0
R149[c]	$OH+ PH \rightarrow H + HPO$	5.25e-13	0.0	2287.58
R151[c]	$OH + P_2O \rightarrow H + P_2O_2$	5.25e-13	0.0	7167.03
R153[c]	$OH + P_2O \rightarrow HOPO + P$	5.25e-13	0.0	6013.62
R155[c]	$OH + P_2O_2 \rightarrow PO + HOPO$	5.25e-13	0.0	6013.62
R157[c]	$OH + H_2POH \rightarrow H_2O + HPOH$	5.25e-13	0.0	823.87
R159[c]	$OH + HPOH \rightarrow H_2O + HPO$	5.25e-13	0.0	1650.14
R161[c]	$HO_2 + PO \rightarrow O_2 + HPO$	5.25e-13	0.0	3396.49
R163[c]	$HO_2 + PO \rightarrow O + HOPO$	5.25e-13	0.0	0.0
R165[a]	$HO_2 + PO \rightarrow OH + PO_2$	3.49e-12	0.0	−251.61
R167[a]	$O_2 + HOPO \rightarrow HO_2 + PO_2$	1.16e-11	0.0	22795.84
R169[c]	$HO_2 + PO_2 \rightarrow O + HOPO_2$	5.25e-13	0.0	0.0
R171[a]	$HO_2 + PO_2 \rightarrow OH + PO_3$	8.3e-13	0.0	0.0
R173[a]	$HO_2 + HOPO \rightarrow OH + HOPO_2$	2.49e-10	0.0	11875.98
R175[a]	$HO_2 + HOPO \rightarrow H_2O_2 + PO_2$	4.15e-12	0.0	11725.02
R177[a]	$HO_2 + HOPO_2 \rightarrow H_2O_2 + PO_3$	4.15e-12	0.0	12379.2
R179[a]	$O_2 + HOPO_2 \rightarrow HO_2 + PO_3$	1.16e-11	0.0	33212.49
R181[c]	$HO_2 + HPO \rightarrow O_2 + HPOH$	5.25e-13	0.0	5135.63
R183[c]	$HO_2 + P \rightarrow O_2 + PH$	5.25e-11	0.0	3420.55
R185[c]	$HO_2 + P \rightarrow OH + PO$	5.25e-11	0.0	922.49
R187[c]	$HO_2 + P_2 \rightarrow OH + P_2O$	5.25e-13	0.0	2549.77
R189[c]	$HO_2 + PH_2 \rightarrow O_2 + PH_3$	5.25e-13	0.0	2639.98
R191[c]	$HO_2 + PH_2 \rightarrow O + H_2POH$	5.25e-13	0.0	0.0
R193[c]	$HO_2 + PH \rightarrow O_2 + PH_2$	5.25e-13	0.0	2629.15
R195[c]	$HO_2 + PH \rightarrow O + HPOH$	5.25e-13	0.0	0.0
R197[c]	$HO_2 + PH \rightarrow OH + HPO$	5.25e-13	0.0	796.2
R199[c]	$HO_2 + P_2O \rightarrow OH + P_2O_2$	5.25e-13	0.0	2265.93
R201[c]	$HO_2 + HPOH \rightarrow O_2 + H_2POH$	5.25e-13	0.0	2658.02
R203[c]	$PO + HOPO_2 \rightarrow PO_2 + HOPO$	5.25e-13	0.0	4895.08
R205[a]	$PO + PO_3 \rightarrow PO_2 + PO_2$	8.3e-13	0.0	0.0
R207[c]	$PO + P_2O \rightarrow PO_2 + P_2$	5.25e-13	0.0	2050.64
R209[c]	$PO + P_2O_2 \rightarrow PO_2 + P_2O$	5.25e-13	0.0	3612.98
R211[c]	$PO + H_2POH \rightarrow HOPO + PH_2$	5.25e-13	0.0	6013.62
R213[c]	$PO + HPOH \rightarrow HOPO + PH$	5.25e-13	0.0	0.0
R215[c]	$PO + HPOH \rightarrow HPO + HPO$	5.25e-13	0.0	5082.71
R217[c]	$PO_2 + HPO \rightarrow H + P_2O_3$	5.25e-13	0.0	6013.62
R219[a]	$PO_2 + HPO \rightarrow PO + HOPO$	3.321e-13	0.0	0.0
R221[c]	$PO_2 + P \rightarrow PO + PO$	5.25e-11	0.0	2472.8
R223[c]	$PO_2 + PH_3 \rightarrow HOPO + PH_2$	5.25e-13	0.0	0.0
R225[c]	$PO_2 + PH_2 \rightarrow HOPO + PH$	5.25e-13	0.0	0.0
R227[c]	$PO_2 + PH \rightarrow PO + HPO$	5.25e-13	0.0	2418.68

Table 3
(Continued)

Reaction number	Forward reaction (2-body)	A	n	E
R229[c]	$PO_2 + PH \rightarrow HOPO + P$	5.25e-13	0.0	36.08
R231[c]	$PO_2 + P_2O \rightarrow PO_3 + P_2$	5.25e-13	0.0	309.1
R233[c]	$PO_2 + P_2O \rightarrow P_2O_3 + P$	5.25e-13	0.0	6013.62
R235[c]	$PO_2 + P_2O_2 \rightarrow PO + P_2O_3$	5.25e-13	0.0	6013.62
R237[c]	$PO_2 + H_2POH \rightarrow HOPO + HPOH$	5.25e-13	0.0	0.0
R239[c]	$PO_2 + H_2POH \rightarrow HOPO_2 + PH_2$	5.25e-13	0.0	6013.62
R241[c]	$PO_2 + HPOH \rightarrow HOPO + HPO$	5.25e-13	0.0	894.83
R243[c]	$PO_2 + HPOH \rightarrow HOPO_2 + PH$	5.25e-13	0.0	0.0
R245[a]	$HOPO + PO_3 \rightarrow PO_2 + HOPO_2$	8.3e-13	0.62	0.0
R247[c]	$HOPO + P_2O \rightarrow HOPO_2 + P_2$	5.25e-13	0.0	18040.85
R249[c]	$HOPO + P_2O_2 \rightarrow HOPO_2 + P_2O$	5.25e-13	0.0	18040.85
R251[c]	$HOPO_2 + P \rightarrow PO + HOPO$	5.25e-11	0.0	3445.8
R253[c]	$HOPO_2 + PH \rightarrow HOPO + HPO$	5.25e-13	0.0	3502.33
R255[a]	$PO_3 + HPO \rightarrow PO + HOPO_2$	3.321e-13	0.0	0.0
R257[c]	$PO_3 + P \rightarrow PO + PO_2$	5.25e-11	0.0	18.04
R259[c]	$PO_3 + PH_3 \rightarrow HOPO_2 + PH_2$	5.25e-13	0.0	0.0
R261[c]	$PO_3 + PH_2 \rightarrow HOPO_2 + PH$	5.25e-13	0.0	0.0
R263[c]	$PO_3 + PH \rightarrow PO_2 + HPO$	5.25e-13	0.0	0.0
R265[c]	$PO_3 + PH \rightarrow HOPO_2 + P$	5.25e-13	0.0	0.0
R267[c]	$PO_3 + P_2O \rightarrow PO_2 + P_2O_2$	5.25e-13	0.0	917.68
R269[c]	$PO_3 + H_2POH \rightarrow HOPO_2 + HPOH$	5.25e-13	0.0	0.0
R271[c]	$PO_3 + HPOH \rightarrow HOPO_2 + HPO$	5.25e-13	0.0	0.0
R273[c]	$HPO + P \rightarrow PO + PH$	5.25e-11	0.0	3474.67
R275[c]	$HPO + PH_2 \rightarrow PO + PH_3$	5.25e-13	0.0	2466.79
R277[c]	$HPO + PH \rightarrow PO + PH_2$	5.25e-13	0.0	2475.21
R279[c]	$HPO + HPOH \rightarrow PO + H_2POH$	5.25e-13	0.0	2489.64
R281[i]	$P + PH \rightarrow H + P_2$	3.66e-11	0.198	−1.166
R283[c]	$P + P_2O \rightarrow PO + P_2$	5.25e-11	0.0	1467.32
R285[c]	$P + P_2O_2 \rightarrow PO + P_2O$	5.25e-11	0.0	2815.58
R287[c]	$P + HPOH \rightarrow HPO + PH$	5.25e-11	0.0	4874.64
R289[c]	$PH_3 + PH \rightarrow PH_2 + PH_2$	5.25e-13	0.0	2759.05
R291[c]	$PH_3 + HPOH \rightarrow PH_2 + H_2POH$	5.25e-13	0.0	2830.01
R293[i]	$PH_2 + PH \rightarrow P + PH_3$	2.51e-21	2.9224	−240.52
R295[c]	$PH_2 + HPOH \rightarrow HPO + PH_3$	5.25e-13	0.0	3825.86
R297[c]	$PH + PH \rightarrow P + PH_2$	5.25e-13	0.0	3317.11
R299[c]	$PH + P_2O \rightarrow HPO + P_2$	5.25e-13	0.0	1721.1
R301[c]	$PH + P_2O_2 \rightarrow HPO + P_2O$	5.25e-13	0.0	2804.75
R303[c]	$PH + H_2POH \rightarrow PH_2 + HPOH$	5.25e-13	0.0	2731.39
R305[c]	$PH + HPOH \rightarrow HPO + PH_2$	5.25e-13	0.0	3675.52
R307[c]	$PH + HPOH \rightarrow P+ H_2POH$	5.25e-13	0.0	3479.48
R309[c]	$P_2O + P_2O \rightarrow P_2 + P_2O_2$	5.25e-13	0.0	18040.85
R311[c]	$HPOH + HPOH \rightarrow HPO + H_2POH$	5.25e-13	0.0	3858.34
R313[j]	$H_3PO_4 \rightarrow HOPO_2 + H_2O$	8.81e4	2.12	19604.37
R315	$He \rightarrow He$	0.0	0.0	0.0

Table 4
Updated PHO Reaction Network for the 3-body Reactions

Reaction Number	Forward Reaction (3-body)	A	n	E	A_∞	n_∞	E_∞
R317	$H + H + M \rightarrow H_2 + M$	2.7e-31	−0.6	0.0	3.31e-06	−1.0	0.0
R319	$H + O + M \rightarrow OH + M$	1.3e-29	−1.0	0.0	1e-11	0.0	0.0
R321	$OH + H + M \rightarrow H_2O + M$	3.89e-25	−2.0	0.0	4.26e-11	0.23	−57.5
R323	$H + O_2 + M \rightarrow HO_2 + M$	2.17e-29	−1.1	0.0	7.51e-11	0.0	0.0
R325	$HO_2 + HO_2 + M \rightarrow H_2O_2 + O_2 + M$	1.9e-33	0.0	−980.0	2.2e-13	0.0	−600.0
R327	$OH + OH + M \rightarrow H_2O_2 + M$	7.97e-31	−0.76	0.0	1.51e-11	−0.37	0.0
R329[i]	$H + PH_2 + M \rightarrow PH_3 + M$	4.320e-24	−2.1662	211.18	1.220e-10	0.200	−8.013
R331[d]	$H + PO_2 + M \rightarrow HOPO + M$	7.95e-17	−4.33	513.28	1.91e-14	1.29	−754.83
R333[d]	$OH + PO_2 + M \rightarrow HOPO_2 + M$	0.28	−8.59	4528.98	2.57e-10	−0.24	0.0
R335[i]	$H + P_2 + M \rightarrow P2H + M$	2.47e-27	−1.23	152.0	1.45e-11	0.54	−58.9
R337[i]	$PO + PO_2 + M \rightarrow P_2O_3 + M$	1.49e-15	−4.25	0.0	2.819e-10	0.167	0.0
R339[c,h]	$H + P + M \rightarrow PH + M$	9.26e-30	−1.1	357.21	1.79e-12	−0.13	459.99
R341[i]	$H + PH + M \rightarrow PH_2 + M$	2.91e-28	−1.10 94.5	7.98e-11	0.222	0.535	
R343[i]	$PH_2 + PH_2 + M \rightarrow P_2H_4 + M$	5.48e-15	−4.836	351.6	1.67e-10	−0.105	45.0
R345[i]	$P_2H_2 + H_2 + M \rightarrow P_2H_4 + M$	6.55e-10	−6.99	6363.0	8.51e-19	2.238	4674.0
R347[c,h]	$OH + P + M \rightarrow HPO + M$	1.241e-25	−1.95	670.0	4.12e-10	0.16	128.41
R349[i]	$P_2O_3 + P_2O_3 + M \rightarrow P_4O_6 + M$	5.925e-18	−2.99	0.0	3.263e-10	0.166	0.0
R351	$O + O + M \rightarrow O_2 + M$	5.21e-35	0.0	−900.0	…	…	…
R353[a]	$H + PO + M \rightarrow HPO + M$	1.241e-25	−1.95	670.0	…	…	…
R355[a]	$H + PO_3 + M \rightarrow HOPO_2 + M$	3.309e-23	−2.37	720.0	…	…	…
R357[c]	$H + HPO + M \rightarrow HPOH + M$	7.549e-26	−1.422	415.5	…	…	…
R359[c]	$H + HPOH + M \rightarrow H_2POH + M$	9.619e-24	−1.885	550.8	…	…	…
R361[a]	$O + PO + M \rightarrow PO_2 + M$	1.103e-22	−2.63	866.0	…	…	…
R363[a]	$O + PO_2 + M \rightarrow PO_3 + M$	8.962e-21	−3.15	946.7	…	…	…
R365[a]	$O + HOPO + M \rightarrow HOPO_2 + M$	8.273e-21	−2.99	1027.0	…	…	…
R367[c]	$O + P + M \rightarrow PO + M$	1.642e-29	−0.747	218.2	…	…	…
R369[a]	$OH + PO + M \rightarrow HOPO + M$	6.894e-27	−2.09	800.7	…	…	…
R371[c]	$OH + PH_2 + M \rightarrow H_2POH + M$	5.715e-29	−1.223	357.2	…	…	…
R373[c]	$OH + PH + M \rightarrow HPOH + M$	2.175e-33	−0.415	121.4	…	…	…
R375[c]	$O + P_2 + M \rightarrow P_2O + M$	7.774e-31	−0.844	265.5	…	…	…
R377[c]	$O + PH + M \rightarrow HPO + M$	2.162e-33	−0.309	97.2	…	…	…
R379[c]	$O + P_2O + M \rightarrow P_2O_2 + M$	5.995e-34	−0.268	84.4	…	…	…
R381[c]	$PO + PO + M \rightarrow P_2O_2 + M$	2.117e-28	−2.077	595.2	…	…	…
R383[c]	$PO + P+M \rightarrow P_2O + M$	2.64e-24	−2.41	690.7	…	…	…
R385[b]	$HOPO_2 + H_2O + M \rightarrow H_3PO_4 + M$	1.35e-07	−7.53	0.0	…	…	…
R387[c]	$P + P + M \rightarrow P_2 + M$	7.191e-27	−1.67	477.2	…	…	…
R389[c]	$P_2 + P_2 + M \rightarrow P4+M$	3.721e-26	−1.867	545.4	…	…	…

ORCID iDs

Elspeth K. H. Lee https://orcid.org/0000-0002-3052-7116
Shang-Min Tsai https://orcid.org/0000-0002-8163-4608
Julianne I. Moses https://orcid.org/0000-0002-8837-0035
John M. C. Plane https://orcid.org/0000-0003-3648-6893
Channon Visscher https://orcid.org/0000-0001-6627-6067
Stephen J. Klippenstein https://orcid.org/0000-0001-6297-9187

References

Alderson, L., Wakeford, H. R., Alam, M. K., et al. 2023, Natur, 614, 664
Angerhausen, D., Ottiger, M., Dannert, F., et al. 2023, AsBio, 23, 183
Asplund, M., Amarsi, A. M., & Grevesse, N. 2021, A&A, 653, A141
Atreya, S. K., Hofstadter, M. H., In, J. H., et al. 2020, SSRv, 216, 18
Bains, W., Pasek, M. A., Ranjan, S., et al. 2023, ESC, 7, 1219
Bains, W., Petkowski, J. J., Seager, S., et al. 2021, AsBio, 21, 1277
Baptista, L., & de Almeida, A. A. 2023, JPCA, 127, 1000
Bauernschmitt, R., & Ahlrichs, R. 1996, CPL, 256, 454
Beiler, S. A., Cushing, M. C., Kirkpatrick, J. D., et al. 2023, ApJL, 951, L48
Benson, S. W., & Buss, J. H. 1958, JChPh, 29, 546
Borunov, S., Dorofeeva, V., Khodakovsky, I., et al. 1995, Icar, 113, 460
Bregman, J. D., Lester, D. F., & Rank, D. M. 1975, ApJL, 202, L55
Burcat, A., & Ruscic, B. 2005, Tech Rep. ANL-05/20, Argonne National Lab.
Cavalié, T., Lunine, J., Mousis, O., & Hueso, R. 2024, SSRv, 220, 8
Chase, M. 1998, NIST-JANAF Thermochemical Tables (4th ed. New York: AIP)
Chen, F., Judge, D. L., Robert Wu, C. Y., et al. 1991, JGRE, 96, 17519
Curtiss, L. A., Redfern, P. C., & Raghavachari, K. 2007, JChPh, 127, 124105
Douglas, K. M., Blitz, M. A., Mangan, T. P., & Plane, J. M. C. 2019, JPCA, 123, 9469
Douglas, K. M., Blitz, M. A., Mangan, T. P., Western, C. M., & Plane, J. M. C. 2020, JPCA, 124, 7911
Douglas, K. M., Gobrecht, D., & Plane, J. M. C. 2022, MNRAS, 515, 99
Edgington, S. G., Atreya, S. K., Trafton, L. M., et al. 1998, Icar, 133, 192
Encrenaz, T., Greathouse, T. K., Marcq, E., et al. 2020, A&A, 643, L5
Fegley, B. J., & Lodders, K. 1994, Icar, 110, 117
Fegley, B. J., & Lodders, K. 1996, ApJL, 472, L37
Fegley, B. J., & Prinn, R. G. 1985, ApJ, 299, 1067
Fletcher, L. N., Orton, G. S., Teanby, N. A., & Irwin, P. G. J. 2009, Icar, 202, 543
Frisch, M. J., Trucks, G. W., Schlegel, H. B., et al. 2016, Gaussian 16 Revision C.01
Fritz, B. K., Lorenz, K., Steinert, W., & Zellner, R. 1982, Physico-Chemical Behavior of Atmospheric Pollutants (Berlin: Springer), 192
Garvin, J. B., Getty, S. A., Arney, G. N., et al. 2022, PSJ, 3, 117
Georgievskii, Y., & Klippenstein, S. J. 2005, JChPh, 122, 194103
Ghail, R., Wilson, C., Widemann, T., et al. 2017, arXiv:1703.09010
Gilbert, R., & Smith, S. 1990, Theory of Unimolecular and Recombination Reactions (Oxford: Blackwell)
Glaude, P., Curran, H., Pitz, W., & Westbrook, C. 2000, PComI, 28, 1749
Glowacki, D. R., Liang, C.-H., Morley, C., Pilling, M. J., & Robertson, S. H. 2012, JPCA, 116, 9545

Greaves, J. S., Richards, A. M. S., Bains, W., et al. 2021, NatAs, 5, 655
Gurvich, L. V., Veyts, I. V., & Alcock, C. B. 1989, Thermodynamic Properties of Individual Substances, Vol. 1 (4th ed.; New York: Hemisphere)
Haworth, N. L., Bacskay, G. B., & Mackie, J. C. 2002, JPCA, 106, 1533
Heays, A. N., Bosman, A. D., & van Dishoeck, E. F. 2017, A&A, 602, A105
Huebner, W. F., & Mukherjee, J. 2015, P&SS, 106, 11
Jayaweera, T. M., Melius, C. F., Pitz, W. J., et al. 2005, CoFl, 140, 103
Kaye, J. A., & Strobel, D. F. 1983, GeoRL, 10, 957
Kaye, J. A., & Strobel, D. F. 1984, Icar, 59, 314
Kurucz, R. L., & Bell, B. 1995, Atomic Line List, Kurucz CD-ROM (Cambridge, MA: Smithsonian Astrophysical Observatory)
Li, C., Ingersoll, A., Bolton, S., et al. 2020, NatAs, 4, 609
Lincowski, A. P., Meadows, V. S., Crisp, D., et al. 2021, ApJL, 908, L44
Lizardo-Huerta, J.-C., Sirjean, B., Verdier, L., Fournet, R., & Glaude, P.-A. 2021, PComI, 38, 719
Lodders, K. 1999, JPCRD, 28, 1705
Lodders, K. 2021, SSRv, 217, 44
Mackie, J. C., Bacskay, G. B., & Haworth, N. L. 2002, JPCA, 106, 10825
Malik, M., Grosheintz, L., Mendonça, J. M., et al. 2017, AJ, 153, 56
McBride, B. J., & Gordon, S. 1992, Tech. Rep. NASA RP-1271, NASA Lewis Research Center, https://ntrs.nasa.gov/search.jsp?R=19930003779
Miles, B. E., Skemer, A. J. I., Morley, C. V., et al. 2020, AJ, 160, 63
Morley, C. V., Skemer, A. J., Allers, K. N., et al. 2018, ApJ, 858, 97
Moses, J. I., Fouchet, T., Bézard, B., et al. 2005, JGRE, 110, E08001
Moses, J. I., Tremblin, P., Venot, O., & Miguel, Y. 2022, ExA, 53, 279
Moses, J. I., Visscher, C., Fortney, J. J., et al. 2011, ApJ, 737, 15
Mousis, O., Lunine, J. I., & Aguichine, A. 2021, ApJL, 918, L23
Nava, D. F., & Stief, L. J. 1989, JPhCh, 93, 4044
Pasek, M. A., Gull, M., & Herschy, B. 2017, ChGeo, 475, 149
Plane, J. M. C., Feng, W., & Douglas, K. M. 2021, JGRA, 126, e29881
Powell, D., Feinstein, A. D., Lee, E. K. H., et al. 2024, Natur, 626, 979
Prajapat, L., Jagoda, P., Lodi, L., et al. 2017, MNRAS, 472, 3648
Prinn, R. G., & Lewis, J. S. 1975, Sci, 190, 274
Quanz, S. P., Ottiger, M., Fontanet, E., et al. 2022, A&A, 664, A21
Ridgway, S., Larson, H., & Fink, U. 1976, in IAU Colloq. 30, Jupiter: Studies of the Interior, Atmosphere, Magnetosphere and Satellites (Cambridge: Cambridge Univ. Press), 384
Ridgway, S. T., Wallace, L., & Smith, G. R. 1976, ApJ, 207, 1002
Rustamkulov, Z., Sing, D. K., Mukherjee, S., et al. 2023, Natur, 614, 659
Sander, S., Friedl, R., Golden, D., et al. 2006, Tech. Rep. JPL-Publ-06-2, Jet Propulsion Laboratory, California Inst. of Tech., https://ntrs.nasa.gov/citations/20090033862
Sousa-Silva, C., Seager, S., Ranjan, S., et al. 2020, AsBio, 20, 235
Stock, J. W., Kitzmann, D., Patzer, A. B. C., & Sedlmayr, E. 2018, MNRAS, 479, 865
Strobel, D. F. 1977, ApJL, 214, L97
Toner, J. D., & Catling, D. C. 2019, GeCoA, 260, 124
Tsai, S.-M., Lee, E. K. H., Powell, D., et al. 2023, Natur, 617, 483
Tsai, S.-M., Lyons, J. R., Grosheintz, L., et al. 2017, ApJS, 228, 20
Tsai, S.-M., Malik, M., Kitzmann, D., et al. 2021, ApJ, 923, 264
Twarowski, A. 1995, CoFl, 102, 41
Villanueva, G. L., Cordiner, M., Irwin, P. G. J., et al. 2021, NatAs, 5, 631
Visscher, C. 2020, JGRE, 125, e06526
Visscher, C., & Fegley, B. J. 2005, ApJ, 623, 1221
Visscher, C., Lodders, K., & Fegley, B. J. 2006, ApJ, 648, 1181
Wang, D., Lunine, J. I., & Mousis, O. 2016, Icar, 276, 21
Wang, D., Miguel, Y., & Lunine, J. 2017, ApJ, 850, 199
Zehe, M. J., Gordon, S., & McBride, B. J. 2002, Tech. Rep. NASA/TP-2001-210959/REV1, NASA Glenn Research Center Cleveland, OH, https://ntrs.nasa.gov/citations/20020036214